RSC Advances

PAPER

View Article Online
View Journal | View Issue

Cite this: *RSC Adv.*, 2025, **15**, 33726

Durian peel–seed biochar for efficient methylene blue removal from water: synthesis, characterization, and adsorption performance

Do Tra Huong,[a] Nguyen Ngoc Phuong Ngan,[a] Duong Thi Tu Anh,[a] Nguyen Dinh Vinh[b] and Vuong Truong Xuan *[b]

Dye contamination in wastewater represents a significant environmental challenge because of the toxic nature and poor biodegradability of these compounds. Developing cost-effective, environmentally friendly adsorbent materials derived from agricultural waste is essential for enhancing wastewater treatment efficiency at a reasonable cost. This study investigated the adsorption capability of methylene blue (MB) from aqueous solutions using activated carbon synthesized from durian shells and seeds (BDSS). The adsorbent was prepared *via* pyrolysis at 500 °C combined with a subsequent hydrothermal treatment. Adsorption experiments were conducted to evaluate key influencing factors and adsorption characteristics. The results revealed that BDSS exhibited a high specific surface area (441.71 $m^2\ g^{-1}$), a porous structure, an iodine number of 589 mg g^{-1}, and a point of zero charge (pH_{pzc}) of 6.47. The adsorption of MB onto BDSS followed the Langmuir isotherm model, achieving a maximum adsorption capacity of 136.99 mg g^{-1}. The process adhered to pseudo-second-order kinetics and was identified as a spontaneous and endothermic reaction. Adsorption was observed to occur on both homogeneous and heterogeneous surface sites through a combination of physical and chemical mechanisms, including electrostatic interactions, hydrogen bonding, π–π interactions, electron donor–acceptor interactions, and pore filling. In addition, an artificial neural network (ANN) model was well established to predict BDSS adsorption performance under varying conditions. The optimal ANN with five input variables, one hidden layer of 11 neurons, and one output neuron showed excellent predictive accuracy (R > 0.99). Initial MB concentration had the most pronounced effect, followed by temperature, adsorbent dosage, contact time, and pH. The method is beneficial for process optimization and engineering applications. Furthermore, BDSS maintained 53.74% of its adsorption capacity after three reuse cycles, demonstrating good reusability. Overall, the findings suggest that BDSS-derived activated carbon is a promising, eco-friendly adsorbent with potential applications in the treatment of dye-contaminated wastewater.

Received 23rd July 2025
Accepted 10th September 2025

DOI: 10.1039/d5ra05313g

rsc.li/rsc-advances

1. Introduction

Methylene blue (MB) is a synthetic cationic dye extensively applied in a variety of industries, including textiles, printing, leather tanning, and paper manufacturing. Due to its highly stable molecular structure, excellent water solubility, and strong dyeing properties, MB is frequently detected in industrial wastewater at significant concentrations, as it is often not completely removed during standard treatment processes. When released into the environment, MB not only causes visible color change in natural bodies of water but also initiates a range of negative ecological and human health effects. Ecologically, MB is capable of inhibiting photosynthesis in aquatic plants, reducing dissolved oxygen, and disrupting normal food chains. In humans, prolonged exposure to MB can lead to serious health issues, including respiratory impairment, nausea, vomiting, headaches, and in severe instances, blindness and nervous system impairment. More recent research has also established the potential genotoxic and carcinogenic activity of this chemical.[1,2] In these situations, effective treatment of MB in wastewater has become an acute environmental problem. Many approaches have been investigated and utilized for the removal or degradation of MB from water sources, including chemical precipitation, oxidation, coagulation, electrochemical treatment, membrane separation, photocatalysis, and ion exchange.[3–6] Among them, adsorption has been extensively recognized as one of the best and economic techniques. Adsorption not only provides high MB removal efficiency but is also characterized by some unique benefits such as low operation cost, simplicity, no toxic by-products, and recoverability of the adsorbent.[7,8] Durian seeds and shells have become potential

[a]*Faculty of Chemistry, Thai Nguyen University of Education, 20 Luong Ngoc Quyen Street, Thai Nguyen City 24000, Vietnam*
[b]*Faculty of Natural Sciences and Technology, TNU-University of Science, Tan Thinh Ward, Thai Nguyen City 24000, Vietnam. E-mail: xuanvt@tnus.edu.vn*

biomass resources for the production of adsorbent materials because they have a high chemical composition. Durian fruit waste mainly consists of cellulose, hemicellulose, lignin, and some organic compounds. Cellulose, as mentioned by Adunphatcharaphon *et al.* (2020),[9] constitutes the highest percentage (about 47%), followed by hemicellulose and lignin, which are about 10% each. Durian waste is thus a great carbon-rich precursor for the synthesis of bio-based adsorbents.

According to the Food and Agriculture Organization (FAO), global commercial production of durian was over 930 000 tons in 2021, ten times what it was in the early 2000s. Thailand, Malaysia, and Indonesia alone produce approximately 866 000 tons of durian waste annually in Southeast Asia,[10] and the global production is even higher, contributing significantly to environmental pollution. In Vietnam, durian production was around 642 000 tons in 2022 and generated approximately 449 400 tons of shell and seed waste.[11] If it is not well managed, the tremendous volume of organic waste can cause significant environmental issues.[12]

The utilization of durian waste for the production of adsorbents not only addresses the problem of agricultural waste pollution but also contributes to the creation of sustainable solutions in wastewater treatment. Current research has been successful in exploring the conversion of biomass and agricultural waste, durian shells included, into green adsorbents. For example, Cai *et al.* (2022)[2] prepared a composite material consisting of durian shell biochar fibers and Fe_3O_4 loaded in a metal–organic framework (MOF) structure, which exhibited excellent dye adsorption capacity and high reusability. All the above results reveal the huge potential of agricultural waste valorization for sustainable and economic dye removal.

In the last few years, numerous studies have focused on the synthesis and application of adsorbent materials for the efficient removal of pollutants from aquatic systems. Activated carbon, natural and modified biochars, metal–organic frameworks (MOFs), and natural or surface-modified clays with high adsorption capacities are the most studied materials.[13–15] Among these, activated carbon is particularly valued because of its low cost, extensive sources of raw materials, ease of preparation, and high regenerability.[16,17] The adsorption capacity of activated carbon is primarily governed by its pore structure, specific surface area, and presence of active surface functional groups.

One of the emerging research fields is the production of activated carbon from renewable raw materials agricultural wastes, such as durian shells, which are abundant, carbon-rich, and environmental-friendly materials. As advocated by Jamnongkan *et al.*,[18] the typical synthesis of activated carbon from durian shells involves two general steps: (1) pyrolysis of raw biomass under oxygen-limited conditions to produce biochar, and (2) chemical activation of the produced biochar, followed by pyrolysis, to produce an ordered porous activated carbon. With high temperature in the initial stage of pyrolysis, hydrogen and oxygen elements of cellulose are favored to decompose into gases, and the resulting product is enriched with carbon. In the second activation process, biochar is mixed with activating agents such as acids (H_2SO_4, H_3PO_4), bases (KOH), or salts and again subjected to heat treatment. Acids donate protons (H^+), whereas bases donate hydroxyl groups (OH^-), which alter surface properties and facilitate pore development in the activated carbon.[19–23] Contact between the activating agents and the carbon matrix produces adsorbents with large surface areas, well-developed pore structure, and strong binding energies for contaminants.

In addition to chemical activation, hydrothermal carbonization (HTC) has also been widely applied for processing biomass into porous carbon materials with high adsorption potential. HTC facilitates the formation of microporous structures, preserves aromatic ring stability, and improves the interaction between the adsorbent and pollutants in aqueous systems.[24,25] Consequently, the combined use of pyrolysis and hydrothermal methods to produce biochar from agricultural waste, such as durian shells, is regarded as a promising approach for creating eco-friendly, high-performance adsorbents.

However, to the best of our knowledge, while numerous studies have reported the preparation of activated carbon and biochar from either durian shells or seeds, very few have explored the combined use of both shells and seeds in adsorbent synthesis. Moreover, no study has yet employed a sequential pyrolysis followed by hydrothermal treatment using a mixture of durian shells and seeds specifically for methylene blue adsorption. Existing research has also not provided a comprehensive evaluation of key aspects such as the physical properties, iodine number, adsorption kinetics, activation energy, thermodynamics, and adsorption mechanisms of MB on carbon materials derived from this combined biomass source. Notably, the application of the Halsey isotherm model, which effectively describes adsorption on heterogeneous surfaces, has not been thoroughly investigated in this context.

In parallel with materials development, recent advances in machine-learning architectures highlight how domain-aware feature extraction and multiscale representation can substantially improve predictive performance on irregular, high-dimensional data. For example, graph-based deep networks equipped with edge-convolution layers and multiscale neighborhoods have achieved accurate segmentation of complex, non-Euclidean point-cloud surfaces; incorporating normal-vector features further enhances sensitivity to subtle geometric patterns, albeit with higher computational load.[26,27] These studies, while developed for human–machine interaction and rehabilitation tasks, underscore generalizable strategies, robust feature learning, density-aware training, and careful accuracy–complexity trade-offs that we also leverage in our ANN analysis for adsorption modeling. Building on these insights, our ANN is configured to capture nonlinear structure–property relationships in MB uptake while remaining computationally efficient for practical use.[26,27]

The present study aims to synthesize activated carbon from a combined mixture of durian shells and seeds, a novel and underexplored approach, using a two-stage process involving pyrolysis and hydrothermal treatment to optimize pore structure and adsorption properties. To date, no published study has simultaneously utilized both durian shells and seeds in this

combined method for methylene blue removal. The specific objectives of this study are to: (i) synthesize and characterize activated carbon derived from durian shells and seeds, with a focus on determining physical properties such as specific surface area, pore structure, iodine index, and surface functional groups. (ii) Evaluate the adsorption efficiency of methylene blue under various experimental conditions. (iii) Analyze the adsorption behavior using isotherm models (Langmuir, Freundlich, Temkin, Elovich, Redlich-Peterson, and Halsey), kinetic models (pseudo-first-order, pseudo-second-order, Elovich, the particle diffusion kinetic model), and thermodynamic parameters ($\Delta G°$, $\Delta H°$, $\Delta S°$) to elucidate the adsorption mechanisms involved.

2. Materials and methods

2.1. Materials

2.1.1. Source and preparation of durian peel and seed. Durian shells and seeds were collected from local markets in Thai Nguyen province, where durian is commonly purchased by residents for consumption. After the edible flesh was used as food, the shells and seeds, by-products typically regarded as low-value agricultural waste, were gathered for use as raw materials in the preparation of biochar. The recovery and utilization of such agricultural residues not only help to reduce the volume of organic waste generated from daily activities but also contribute to the development of eco-friendly adsorbent materials for environmental remediation applications.

2.1.2. Chemicals. All chemicals used in the experiments were of analytical reagent grade (PA) and were supplied by Merck. The reagents included methylene blue, NaOH solution, HNO_3 solution, and ethanol (C_2H_5OH).

2.2. Synthesis of studied materials

The preparation of biochar from durian shells and seeds (DSS) was carried out using a combined pyrolysis and hydrothermal method as follows: the durian shells and seeds were first thoroughly washed with water to remove dust and inorganic impurities, then sun-dried for 24 hours. The materials were subsequently oven-dried at 80 °C for 24 hours. After drying, the shells and seeds were mixed at a mass ratio of 2 : 1 (shells to seeds), then cut into small pieces and ground to a particle size of less than 4 mm. The mixture samples were carbonized in a muffle furnace at 400, 500, and 600 °C for 3 h, with a heating rate of 5 °C min^{-1}. The carbonization was carried out in covered ceramic crucibles to minimize oxygen intrusion, thereby ensuring an oxygen-limited environment favorable for biochar formation. After pyrolysis, the resulting material was cooled, transferred into an autoclave containing distilled water, sealed, and subjected to hydrothermal treatment at 200 °C for 6 h. The hydrothermal process was conducted under self-generated pressure conditions, ranging from approximately 1.5 to 2.0 MPa. The final product was filtered, oven-dried at 60–80 °C until a constant weight was achieved, ground into fine powder, and stored in a desiccator.

The biochar samples produced from durian shells and seeds at pyrolysis temperatures of 400 °C, 500 °C, and 600 °C were labeled as BDSS4, BDSS45, and BDSS6, respectively. All samples were stored in sealed containers and kept in a desiccator. An amount of 0.05 g of each material, BDSS4, BDSS5, and BDSS6, was added to separate Erlenmeyer flasks containing 20 mL of MB solution with an accurately determined initial concentration of 50 mg L^{-1} at pH 7. The mixtures were then shaken using a mechanical shaker at 300 rpm for 60 minutes under ambient temperature conditions (25 ± 1 °C). After the adsorption process, the solutions were centrifuged at 4000 rpm for 15 minutes. The supernatant was collected using a micropipette to determine the residual concentration of MB.

The calculated adsorption efficiencies of MB onto BDSS4, BDSS5, and BDSS6 were 80.40%, 91.15%, and 85.06%, respectively (Fig. S1, see SI). The results indicate that BDSS5 exhibited the highest adsorption efficiency for MB (91.15%). This can be explained by the fact that during the calcination of the durian shell and seed materials at 600 °C, partial decomposition may have occurred, forming ash and reducing the carbon content, which in turn decreased the adsorption efficiency. Therefore, BDSS5 was selected as the material for further adsorption studies of MB in aqueous solutions. From this point on, this material is denoted as BDSS.

2.3. Characterization of studied materials

The surface morphology of DSS and BDSS, both before and after adsorption, was examined using scanning electron microscopy (SEM) on a JSM-6510LV instrument (Jeol, Tokyo, Japan). The elemental composition of DSS and BDSS was analyzed by energy-dispersive X-ray spectroscopy (EDS) using the same SEM system. In addition, the surface functional groups of BDSS before and after adsorption were identified through Fourier-transform infrared spectroscopy (FT-IR) using a Neus 670 spectrometer (Nicolet, Brighton, MO, USA). The crystalline structure of BDSS was characterized by X-ray diffraction (XRD) using an Equinox 5000 instrument (Thermo Science, Paris, France), and by Raman spectroscopy with a Micro-Raman LAB RAM-1B system (Jobin-Yvon, France). The specific surface area of BDSS was determined by the Brunauer–Emmett–Teller (BET) method using a Micromeritics-3030 analyzer (USA).

2.4. Determination of the point of zero charge (pH_{pzc}) of the material

A series of 0.1 M NaCl solutions with initial pH values (pH_i) ranging from 1 to 10 was prepared. Ten 100 mL Erlenmeyer flasks were set up, each containing 0.05 g of BDSS material. Subsequently, 100 mL of NaCl solution at the corresponding initial pH was added to each flask. The mixtures were left undisturbed for 48 hours to reach equilibrium, after which the suspensions were filtered, and the final pH (pH_f) of each solution was measured. The pH difference (ΔpH) was calculated using the equation $\Delta pH = pH_f - pH_i$. A graph of ΔpH *versus* pH_i was plotted, and the point at which the curve intersects the *x*-axis (where $\Delta pH = 0$) was identified as the point of zero charge (pH_{pzc}) of the material.

2.5. Batch study on factors affecting methylene blue adsorption by BDSS

To ensure reproducibility, each experiment assessing the adsorption capacity of BDSS for methylene blue (MB) was conducted in triplicate under identical conditions. The reported results represent the average of the three independent trials.

The concentration of methylene blue (MB) was analyzed and determined using the UV-Vis molecular absorption spectrophotometry method on a UH5300 spectrophotometer (Hitachi, Japan). The adsorption efficiency of MB by BDSS was calculated using the following equation:

$$H = \frac{(C_0 - C_{cb})}{C_0} \times 100 \quad (1)$$

where, H is the adsorption efficiency (%), C_0 is the initial concentration of the solution (mg L^{-1}), C_e is the equilibrium concentration of the solution (mg L^{-1}).

2.5.1. Effect of pH. An amount of 0.05 g of BDSS was placed in a 100 mL Erlenmeyer flask, followed by the addition of 20 mL of MB solution with an accurately prepared initial concentration of 50.00 mg L^{-1}. The pH of the solutions was adjusted within the range of 3 to 10 using 0.1 M HCl and 0.1 M NaOH solutions. The mixtures were agitated on a shaker at 300 rpm for 60 minutes at room temperature (25 ± 1 °C). After the adsorption process, the suspensions were centrifuged at 4000 rpm for 15 minutes to separate the solid phase, and the residual concentration of MB in the supernatant was subsequently determined by using the UV-Vis method.

2.5.2. Effect of contact time. Adsorption is a dynamic equilibrium process, where the adsorbate requires a certain period to reach adsorption equilibrium. Insufficient contact time may result in incomplete adsorption, whereas excessive contact time could lead to desorption and unnecessary time consumption. Therefore, following the pH study, the effect of contact time on the adsorption equilibrium was investigated.

A total of 0.05 g of BDSS was added to 100 mL Erlenmeyer flasks containing 20 mL of MB solutions at accurately prepared concentrations of 50 mg L^{-1}, 75 mg L^{-1}, and 100 mg L^{-1}. All solutions were adjusted and maintained at pH 7. The adsorption experiments were conducted by shaking at 300 rpm for varying contact times: 30, 60, 90, 120, 150, 180, and 210 minutes at room temperature (25 ± 1 °C). At each designated time interval, samples were withdrawn and centrifuged at 4000 rpm. The supernatants were carefully collected using a micropipette, and the residual MB concentrations were measured to assess adsorption performance over time.

2.5.3. Effect of adsorbent dosage. A series of BDSS samples with varying masses ranging from 0.01 g to 0.125 g were introduced into separate 100 mL Erlenmeyer flasks. Each flask was then filled with 20 mL of MB solution at an accurately determined initial concentration of 50 mg L^{-1}. The pH of all solutions was adjusted and maintained at 7. The adsorption experiments were performed by shaking the mixtures at 300 rpm for 60 minutes at room temperature (25 ± 1 °C). After adsorption, the mixtures were centrifuged at 4000 rpm for 15 minutes to separate the solids, and the residual MB concentration in the supernatant was subsequently determined.

2.5.4. Effect of temperature. A set of 100 mL Erlenmeyer flasks was prepared, each containing 0.05 g of BDSS and 20 mL of MB solution with an accurately prepared initial concentration of 100.00 mg L^{-1}. The pH of all solutions was adjusted to 7 using 0.1 M NaOH and 0.1 M HNO_3 solutions. The adsorption experiments were carried out on a thermostatic magnetic stirrer at stirring speeds of 300 rpm for contact times ranging from 30 to 120 minutes. The tests were conducted at different temperatures: 303 K, 313 K, and 323 K. After adsorption, the suspensions were centrifuged to remove the solids, and the residual MB concentration in the supernatant was measured.

2.5.5. Effect of initial MB concentration. Each 100 mL Erlenmeyer flask was loaded with 0.05 g of BDSS and 20 mL of MB solution with initial concentrations ranging from 50 to 500 mg L^{-1} (accurately prepared). The pH of all solutions was adjusted and maintained at 7 throughout the experiments. The adsorption was performed by shaking the mixtures at 300 rpm for 60 minutes at room temperature (25 ± 1 °C). After adsorption, the mixtures were centrifuged at 4000 rpm for 15 minutes. The supernatants were collected using a micropipette, and the residual concentrations of MB were determined to evaluate the adsorption capacity at different initial concentrations.

2.5.6. ANN-based simulation of methylene blue adsorption onto durian-derived activated carbon. Artificial neural network (ANN) modeling was employed to simulate the adsorption behavior of methylene blue (MB) on activated carbon derived from durian waste. The five input variables were pH, contact time, adsorbent dose, initial MB concentration, and temperature. The whole dataset was divided at random into three sets: 70% for model training, 15% for validation, and 15% for testing. The ANN architecture consisted of three layers: an input layer comprising five neurons (one for each independent variable), a single hidden layer, and an output layer with one neuron that represented the estimated MB removal efficiency. The number of hidden layer neurons was optimized using a trial-and-error method, varying from 5 to 20 neurons, to select the best configuration. Training was performed through the Levenberg–Marquardt backpropagation algorithm (trainlm) with a fast convergence rate and function approximation ability chosen to perform the training. Gradient descent with momentum (learngdm) was utilized as the adaptation learning rule to enhance the speed of learning and avoid local minima trapping. Regarding the activation functions, the hidden layer utilized the hyperbolic tangent sigmoid function (tansig) to leverage its nonlinear mapping characteristics when handling normalized input data. The output layer utilized a linear activation function (purelin) to facilitate continuous prediction of the output. The model's predictive ability was established through comparison of the ANN-derived outputs with experimental outputs. Performance metrics involved the mean squared error (MSE), Pearson correlation coefficient (R), and the coefficient of determination (R^2), which are calculated below:

$$\mathrm{MSE} = \frac{1}{N}\sum_{i}^{N}\left(y_{\mathrm{prd},i} - y_{\mathrm{exp},i}\right)^2 \quad (2)$$

$$R = \frac{\sum_{i}^{N} \left(y_{\exp,i} - y_{\exp,m}\right)\left(y_{\mathrm{prd},i} - y_{\mathrm{prd},m}\right)}{\sqrt{\sum_{i}^{N} \left(y_{\exp,i} - y_{\exp,m}\right)^2} \times \sqrt{\sum_{i}^{N} \left(y_{\mathrm{prd},i} - y_{\mathrm{prd},m}\right)^2}} \quad (3)$$

All modeling and computations involved in these equations are the experimental observed value $y_{\exp,i}$, predicted value $y_{\mathrm{prd},i}$, mean of observed values $y_{\exp,m}$, mean of predicted values $y_{\mathrm{prd},m}$ and number of samples N. All analysis and modeling were conducted using MATLAB R2018a and its Neural Network Toolbox.

2.6. Adsorption isotherms, kinetics, and thermodynamics

2.6.1. Adsorption isotherms. To accurately describe the adsorption behaviour of MB onto biochar, various adsorption isotherm models were employed. These models help to understand the interaction between the adsorbate and the adsorbent surface, providing insights into adsorption capacity, surface heterogeneity, and the mechanism of adsorption. The Langmuir model assumes monolayer adsorption on a homogeneous surface, whereas the Freundlich model accounts for multilayer adsorption on heterogeneous surfaces. The Temkin, Elovich, Redlich–Peterson, and Halsey models further refine the analysis by incorporating factors such as temperature effects, surface heterogeneity, and empirical fitting parameters. The Langmuir equation is founded on monolayer adsorption onto a homogeneous surface and is expressed by the equation $C_0/q_e = 1/(q_{max} \times b) + C_e/q_{max}$, where q_e and q_{max} are the equilibrium and maximum adsorption capacities (mg g^{-1}) and b is the constant of Langmuir. The favorability of adsorption is expressed by the separation factor $R_L = 1/(1 + b \times C_0)$ with $0 < R_L < 1$ for favorable adsorption. The Freundlich model describes multilayer adsorption onto heterogeneous surfaces and is expressed as $\ln q_e = \ln K_F + (1/n) \ln C_e$, where n (typically > 1) is the adsorption intensity and K_F is the Freundlich constant. The Temkin model, expressed as $q_e = B \ln K_T + B \ln C_e$ considers indirect adsorbate–adsorbent interactions, and B is the Temkin constant, whereas K_T is the binding constant. The Elovich equation, $\ln(q_e/C_e) = \ln K_E\, q_m - q_e$, is used to describe chemisorption on extremely heterogeneous surfaces, with K_E being the Elovich constant and q_m the maximum adsorption capacity. The Redlich–Peterson model, with contributions of Langmuir and the Freundlich models, is given as $\ln(C_e/q_e) = \beta \ln C_e - \ln A$, with A and β being empirical constants. Finally, the Halsey model, expressed as $q_e = (1/n_H) I_n(K_H - 1/n_H) \ln C_e$, is suitable for multilayer adsorption on a heterogeneous surface, where n_H and K_H are model constants. C_e is the MB solution equilibrium concentration in all models.

2.6.2. Adsorption kinetics. Kinetic studies provide valuable insights into the adsorption mechanism and allow for the identification of potential rate-controlling steps, such as chemical reactions and mass transport processes.[28] While several kinetic models are available, the pseudo-first-order (PFO) and pseudo-second-order (PSO) rate equations are the most frequently employed in adsorption research.[29] In this study, both the pseudo-first-order and pseudo-second-order models were applied. Additionally, to determine if the adsorption process is governed by diffusion, the particle diffusion kinetic model[30] was also utilized.

$$\ln(q_e - q_t) = \ln(q_e) - k_1 t \quad (4)$$

$$\frac{t}{q_t} = \frac{1}{k_{2q_e^2}} + \frac{1}{q_e} t \quad (5)$$

$$q_t = K_{dif}\, t^{0.5} + C_i \quad (6)$$

$$\ln(1 - F) = -K_{fd} \cdot t \quad (7)$$

where t represents the contact time (minutes), k_1 is the first-order rate constant (min^{-1}), and k_2 is the second-order rate constant (min^{-1} L mg^{-1}). q_t is the adsorption capacity at time t, and q_e is the adsorption capacity at equilibrium. K_{dif} and K_{fd} are the constants for intra-particle diffusion and film diffusion rate, respectively. F represents the fraction of solute adsorbed at time t (minutes), where $F = q_t/q_e$ denotes the fractional amount of solute at equilibrium.

2.6.3. Adsorption thermodynamics. The thermodynamic parameters governing the adsorption of MB onto BDSS were evaluated by calculating the standard Gibbs free energy (ΔG°), standard enthalpy (ΔH°), and standard entropy (ΔS°) using the following equations:where R is the universal gas constant (8.314 J mol^{-1} K^{-1}), T is the adsorption temperature in Kelvin, and K_D is the thermodynamic equilibrium constant, which was derived according to the following relationship:

$$\Delta G^\circ = -RT \ln K_D \quad (8)$$

$$\ln\ K_D = -\frac{\Delta G^\circ}{RT} = -\frac{\Delta H^\circ}{RT} + \frac{\Delta S^\circ}{R} \quad (9)$$

where q represents the amount of MB adsorbed, and C_{cb} is the concentration of MB in the solution at equilibrium.

$$K_D = \frac{q}{C_{cb}} \quad (10)$$

2.6.4. Activation energy. To calculate the activation energy from the adsorption kinetics, the value of h is initially determined using the following equation:

$$h = \frac{1}{b} \quad (11)$$

where b is the coefficient in the second-order rate equation. The parameter h represents the initial adsorption rate (mg g^{-1} min) in the PSO model. It describes the adsorption rate at the very beginning of the process.

Subsequently, the activation energy (E) is computed using the equation:

$$E = RT \times (\ln h - \ln k) \quad (12)$$

where R is the universal gas constant ($R = 8.314 \times 10^{-3}$ kJ mol^{-1} K), T is the temperature (K), and k is the second-order rate constant. eqn (11) was chosen to determine the activation

energy as it enables the estimation of the energy barrier of the adsorption process based on the temperature dependence of the rate constant (k) and the initial adsorption rate (h). This approach is particularly useful when analyzing the thermodynamic feasibility and nature of the adsorption mechanism.

2.7. Material reusability

The regeneration of BDSS after adsorption was performed by washing the spent material with 70% ethanol (C_2H_5OH), followed by thorough rinsing with distilled water and subsequent drying. For the reuse experiments, 100 mL Erlenmeyer flasks were prepared, each containing 0.05 g of the regenerated BDSS and 20 mL of MB solution at a precisely controlled concentration of 50 mg L^{-1}. The pH of each solution was adjusted to 7. The adsorption process was carried out by shaking the mixtures at 300 rpm for 60 minutes at room temperature (25 ± 1 °C). After adsorption, the suspensions were centrifuged at 4000 rpm for 15 minutes to separate the solid phase, and the residual MB concentration in the supernatant was determined.

3. Results and discussion

3.1. Physicochemical properties of activated carbon

3.1.1. SEM analysis. The SEM images of DSS and BDSS materials are presented in Fig. 1. As observed, the surface morphology of BDSS underwent significant changes compared to that of DSS. Specifically, Fig. 1a shows that DSS exhibits a relatively smooth, coarse, and poorly porous surface. In contrast, after undergoing pyrolysis and hydrothermal treatment (Fig. 1b), BDSS developed a highly porous structure characterized by thin, wrinkled, and layered plate-like fragments stacked irregularly. This morphological transformation created numerous voids and cavities on the surface, suggesting improved potential for adsorption applications.

This phenomenon can be explained by the material evolution during the pyrolysis stage, where the decomposition of hemicellulose and cellulose led to the formation of a rigid carbon framework with an initially heterogeneous network. Simultaneously, the release of gases such as CO_2 and H_2O during pyrolysis contributed to the initial pore formation within the structure.

During the hydrothermal treatment under elevated pressure and increased water temperature, the carbon structure undergoes expansion and exfoliation, creating internal pores without collapsing the overall framework. Simultaneously, incompletely carbonized substances remaining from the pyrolysis stage continue to hydrolyze and dissolve during the hydrothermal process, further contributing to the enhanced porosity of BDSS.

As illustrated in Fig. 1c, the surface of BDSS after adsorption becomes noticeably smoother. Many of the pores, cavities, and surface grooves are partially or fully filled. The material also shows thicker and broader fragments, and the structure appears more agglomerated compared to the initial adsorbent.

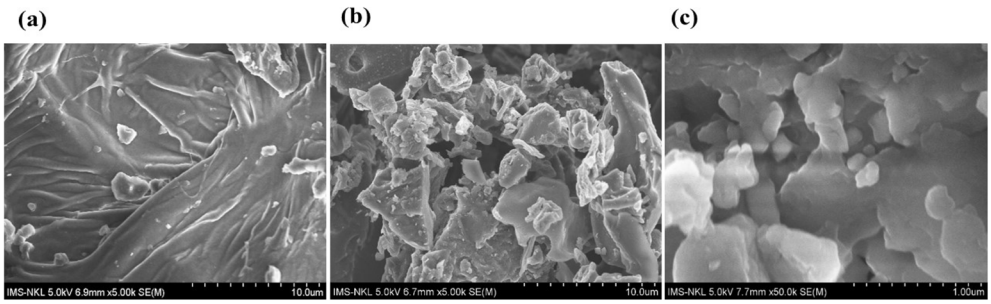

Fig. 1 SEM image of DSS (a), BDSS before adsorption (b) and after adsorption MB (c).

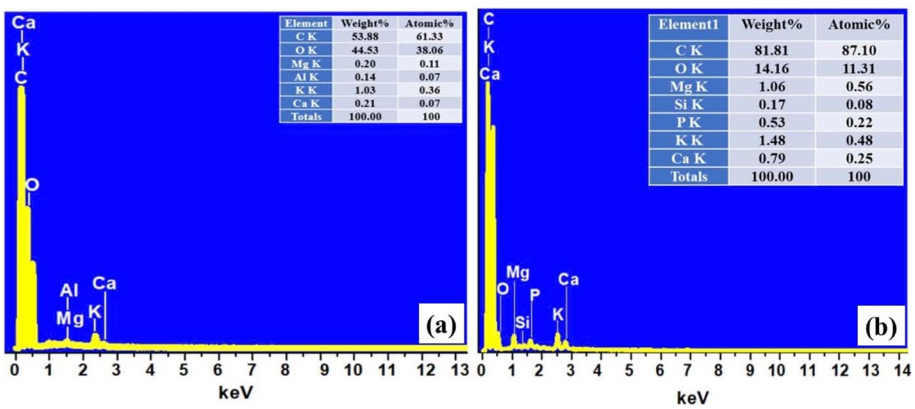

Element	Weight%	Atomic%
C K	53.88	61.33
O K	44.53	38.06
Mg K	0.20	0.11
Al K	0.14	0.07
K K	1.03	0.36
Ca K	0.21	0.07
Totals	100.00	100

Element1	Weight%	Atomic%
C K	81.81	87.10
O K	14.16	11.31
Mg K	1.06	0.56
Si K	0.17	0.08
P K	0.53	0.22
K K	1.48	0.48
Ca K	0.79	0.25
Totals	100.00	100

Fig. 2 EDS spectra of DSS (a) and BDSS (b).

These morphological changes provide clear evidence that methylene blue has been successfully adsorbed onto the BDSS surface.

3.1.2. EDS analysis. The elemental composition of the BDSS material, as determined by energy-dispersive X-ray spectroscopy (EDS), is presented in Fig. 2. The results indicate that BDSS possesses a high carbon content, accounting for 81.81% by weight and 87.10% by atomic percentage, while the oxygen content is relatively low, with values of 14.16% by weight and 11.31% by atomic percentage. In addition to carbon and oxygen, trace amounts of other elements such as Mg, Si, P, K, and Ca were also detected, though their concentrations were minimal.

Comparatively, the carbon content of BDSS is significantly higher than that of the original DSS material (53.88% by weight), while the oxygen content in BDSS is substantially lower than that in DSS (44.53% by weight), as shown in Fig. 2a and b.

This shift in elemental composition can be attributed to the pyrolysis and hydrothermal treatment processes, during which a portion of oxygen was removed in the form of gaseous by-products, and non-carbonaceous compounds were decomposed. As a result, the carbon content increased while the oxygen content decreased in the final material. These EDS findings suggest that BDSS, with its carbon-rich composition and reduced oxygen functionality, holds considerable potential as an efficient adsorbent for removing pollutants from aqueous environments.

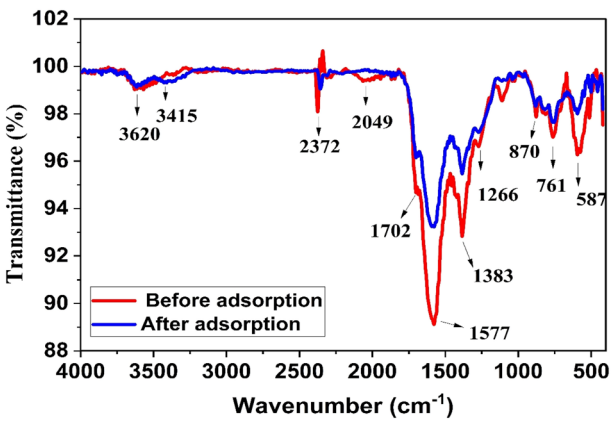

Fig. 3 FT-IR Spectra of BDSS before and after adsorption.

3.1.3. FT-IR analysis of the studied material. The surface functional groups of BDSS before and after adsorption of MB were analyzed using Fourier-transform infrared spectroscopy (FT-IR). The FT-IR spectra and corresponding analysis are presented in Fig. 3 and Table 1. As shown, the FT-IR spectrum of BDSS after adsorption exhibited notable changes, including the disappearance of some characteristic peaks and the emergence of new absorption bands.

Before adsorption, the FTIR spectrum of DBSS exhibited some characteristic absorption bands. Specifically, a sharp peak at almost 3620 cm^{-1} may be termed stretching vibrations of free hydroxyl groups (–OH) or physically adsorbed water on the material surface. The band at 1383 cm^{-1} may be most likely associated with C–H group bending vibrations or the symmetric stretching of carboxylate groups ($–COO^-$). Also apparent was a series of weaker absorption bands at other wavenumbers that were indicative of the intrinsic characteristics of the original DBSS material.

After MB adsorption, FTIR of DBSS revealed the appearance of a new sharp peak at *ca.* 1577 cm^{-1}, which is generally assigned to C=C bond stretching modes of the aromatic rings of the methylene blue molecule. The occurrence of the peak unambiguously proves that MB molecules were, indeed, adsorbed on the surface of the material. Simultaneously, there was a minimal decrease in the intensity of the hydroxyl (–OH) band at 3620 cm^{-1}, which shows hydroxyl groups can be engaged in the adsorption process *via* hydrogen bonding or electrostatic interactions with MB.

The comparative examination of FTIR spectra prior to and following adsorption showed minor wavenumber shifts and changes in the intensity of some peaks, suggesting that surface functional groups of the DBSS material participated in the adsorption process. These observations suggest that the adsorption process of MB onto DBSS may be a synergy of physical adsorption (based on hydrogen bonding and van der Waals forces) and chemical adsorption (through specific interaction between active functional groups on the material surface and the functional groups of MB).

The combined evidence from both the SEM images (Fig. 1c) and the FT-IR spectra (Fig. 3) confirms the successful adsorption of methylene blue onto BDSS. In addition, the FT-IR and EDS analyses consistently demonstrate that carbon and oxygen are the primary elemental components of the BDSS material.

Table 1 FT-IR spectral analysis of BDSS[31]

Wavenumber (cm^{-1})	Functional groups	Assignment
3620	–OH (hydroxyl)	Stretching vibration of free hydroxyl groups, possibly from surface hydroxyls on the carbon structure
1702	C=O (carbonyl)	Stretching vibration of carbonyl groups from carboxylic acids, esters, ketones *etc.*
1577	C=C (aromatic ring or double bond)	Stretching vibration of aromatic rings or C=C double bonds
1383	Methyl ($–CH_3$)	Symmetrical bending vibration or the symmetric stretching of carboxylate groups ($–COO^-$)
1266	C–O (ester, ether, alcohol, phenol)	Stretching vibration
870	C–H	Out-of-plane bending vibration in the aromatic ring
<800		Oxides or salts of K, Mg, Ca, P, Si

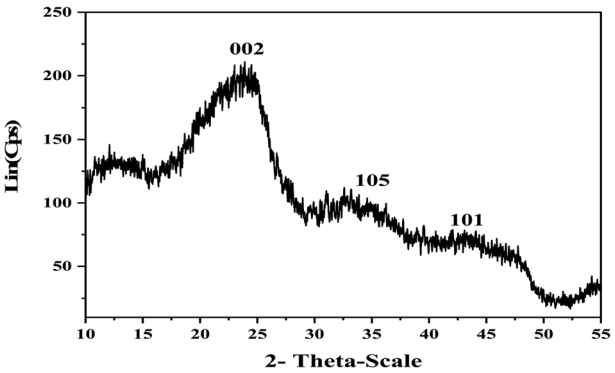

Fig. 4 XRD Diffraction Pattern of BDSS.

3.1.4. X-ray diffraction (XRD) analysis. X-ray diffraction (XRD) analysis was employed to investigate the crystalline structure of the BDSS material. The XRD pattern, recorded over a 2θ range of 0° to 55°, is presented in Fig. 4. The diffraction profile reveals distinct peaks at $2\theta = 23.98°$, 36.63°, and 44.38°, which confirm the presence of carbonaceous phases. The broad diffraction bands observed in the pattern indicate a low degree of crystallinity, characteristic of disordered carbon structures typically formed during pyrolysis and hydrothermal treatment.

The broad diffraction peak at $2\theta = 23.98°$ corresponds to the (002) plane of hexagonal carbon structures, as referenced by JCPDS card no. 50-0926. The weaker peak at $2\theta = 36.63°$ is attributed to the (105) plane of crystalline graphite (JCPDS card no. 721-616). Additionally, the peak observed at $2\theta = 44.38°$ is assigned to the 10 plane, which represents an overlap of the (100) and (101) planes, commonly associated with micro-graphitic layers that lack an ordered stacking arrangement.[31]

These findings collectively indicate that the BDSS material primarily exhibits amorphous carbon characteristics with some degree of graphitization resulting from the combined pyrolysis and hydrothermal processes.

3.1.5. Raman spectroscopy. The Raman spectrum of the BDSS material exhibits three prominent characteristic peaks: the D-band at 1350 cm^{-1}, the G-band at 1620 cm^{-1}, and the 2D-band at 2717 cm^{-1}, as shown in Fig. 5. These peaks are well-known signatures associated with graphitic carbon structures.[32]

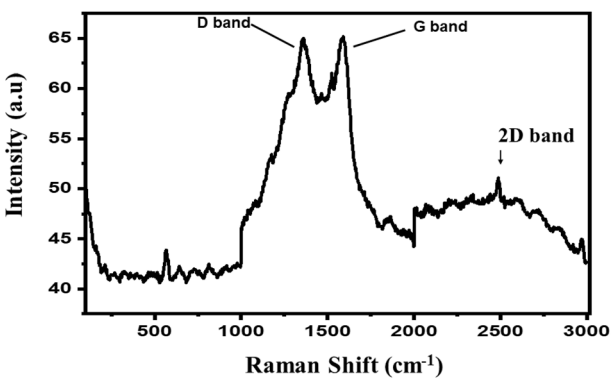

Fig. 5 Raman spectrum of BDSS.

The D-band is typically linked to the vibrational modes of carbon atoms within disordered or defect-rich regions, commonly observed in amorphous graphite-like carbon. In contrast, the G-band is associated with the in-plane stretching vibrations of sp^2-hybridized carbon atoms, indicative of more ordered graphitic domains. The 2D-band (also referred to as the G′ band) provides insight into the degree of crystallinity and stacking order within the carbon material. In this study, the 2D-band appears as a weak, broad feature, suggesting a low-intensity signal and a relatively limited degree of graphitic layer stacking.[33]

According to Wang *et al.* (2019),[34] the intensity ratio of the D and G bands (I_D/I_G) served as a reliable indicator of the degree of graphitization in carbonaceous materials. As illustrated in Fig. 5, the calculated I_D/I_G ratio was 0.89, which suggested that the BDSS material possessed a moderately high degree of graphitization.

3.1.6. BET surface area analysis. The nitrogen adsorption–desorption isotherm of the BDSS material is presented in Fig. 6. The obtained isotherm is classified as type IV with an H4 hysteresis loop, which is characteristic of mesoporous materials where capillary condensation typically occurs. The presence of an H4 hysteresis loop further suggests that the material contains both micropores and mesopores.

The adsorption behavior observed in the relative pressure range (P/P_0) of 0.40 to 0.90 indicates the dominance of mesopores within the BDSS structure. Additionally, the sharp increase in adsorption at P/P_0 values greater than 0.90 corresponds to the presence of macropores or larger pore channels. These features collectively suggest that the BDSS material predominantly possesses a mesoporous architecture.

BET surface area analysis revealed that the specific surface area of BDSS is 441.71 $m^2\ g^{-1}$, with a pore volume of 0.0735 $cm^3\ g^{-1}$ and an average pore diameter of approximately 4.88 nm. These findings indicate that BDSS exhibits considerable porosity and surface area, supporting its potential as an effective adsorbent for pollutant removal from aqueous environments.

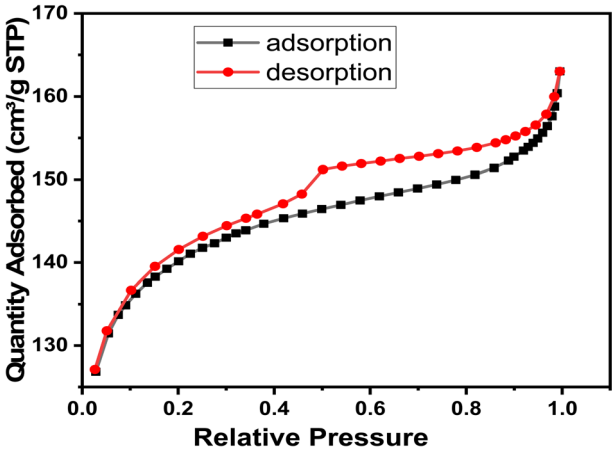

Fig. 6 Nitrogen adsorption–desorption isotherm curve of BDSS.

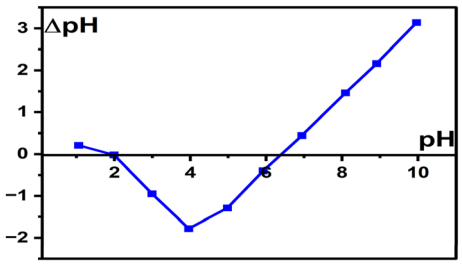

Fig. 7 Determination of the point of zero charge (pH_{pzc}) of BDSS.

3.1.7. Point of zero charge (pH_{pzc}). The point of zero charge (pH_{pzc}) of the BDSS material is presented in Fig. 7. Based on the results, the pH_{pzc} of BDSS was determined to be 6.47. This value is consistent with the findings reported by Ngabura *et al.*,[35] who observed a pH_{pzc} of 6.5 for activated carbon synthesized from durian shells. The pH_{pzc} value indicates that the surface of BDSS carries a positive charge when the solution pH is lower than 6.47, whereas the surface becomes negatively charged when the solution pH exceeds this value. This surface charge behavior is critical in influencing the adsorption interactions between BDSS and ionic species in aqueous environments.

3.1.8. Physical properties of the biochar. The key physical properties of BDSS were determined and are summarized in Table 2. The results indicate that the synthesized biochar possesses low ash content, moderate moisture content, and low bulk density, suggesting that BDSS is lightweight and porous. These characteristics reflect favorable physical attributes, making BDSS a suitable candidate for use as an adsorbent in water pollution treatment applications.

The iodine number, which represents the adsorption capacity of porous materials, particularly activated carbon and highly microporous adsorbents, is a critical parameter for evaluating adsorbent performance. The iodine number of BDSS was measured to be 589 mg g^{-1}. This value falls within the practical range for adsorbents used in environmental applications (500–1200 mg g^{-1}), confirming that BDSS possesses a well-developed porous structure and exhibits good adsorption potential (Table 2).

3.2. Effect of operational parameters

To ensure reproducibility, all adsorption experiments for methylene blue (MB) using BDSS material were conducted in triplicate under identical conditions. The reported results represent the average values obtained from these three independent experiments.

Table 2 Physical properties of BDSS

Physical properties	BDSS
Ash content (%)	6.42 ± 0.05
Moisture content (%)	4.94 ± 0.05
Bulk density (g cm^{-3})	0.81 ± 0.04
Iodine number (mg kg^{-1})	589 ± 1

3.2.1. Effect of pH. The procedure for investigating the influence of pH on the MB adsorption capacity of BDSS material was performed as described in Section 2.4.1. The experimental outcomes are illustrated in Fig. 8 and S2 (SI). The results indicated that pH had a minimal effect on the adsorption efficiency of MB. Specifically, when the pH ranged from 3 to 10, the adsorption efficiency varied only slightly, from 90.90% to 94.18%. This observation can be explained by the nature of MB, which is a cationic dye that predominantly exists as positively charged ions (MB^+) across a wide pH range. Within both acidic and alkaline environments, MB retains its molecular structure and charge state, rendering its adsorption less sensitive to pH variations compared to anionic or amphoteric adsorbates.

Moreover, FT-IR spectral analysis confirmed that BDSS was abundant with hydroxyl (–OH), carboxylate ($–COO^-$), and carbonyl (C=O) functional groups. These functional groups were susceptible to protonation and deprotonation depending on the pH of the solution. In addition, the porous structure and high surface activity of BDSS assist in maintaining a high adsorption affinity towards MB. It is also likely that the strong hydrophobic interactions between MB and BDSS are the major contributors, which is a common mechanism of the physical adsorption of organic molecules on the surface of the adsorbent.[36]

Besides, MB adsorption by BDSS is regulated by over one mechanism, not merely electrostatic forces, but also π–π stacking interaction between the conjugated C=C and N=C bonds of the aromatic rings of the MB molecules.[37] Based on the data presented in Fig. 2, and 14 and the point of zero charge (pH_{pzc}) of BDSS, calculated to be 6.47 (Fig. 7), pH 7 was used as the optimal condition for MB adsorption onto BDSS.

This finding is consistent with that of Nurul Syuhada Sulaiman *et al.*,[38] who had analyzed the adsorption of MB onto biochar derived from cassava stems. In their study, the adsorption efficiency remained high (93.57% to 99.82%) across the pH range of 3–10. Similarly, Jinlong Wang *et al.*[39] observed that MB adsorption onto coal-based activated carbon reached a maximum efficiency of 96.4% at pH 6 and remained stable at higher pH values. The results also align with those of Buddhabhushan Salunkhe,[40] who investigated the adsorption of MB onto a superabsorbent hydrogel based on sodium styrene sulfonate (NaSS) monomer. In that study, MB adsorption

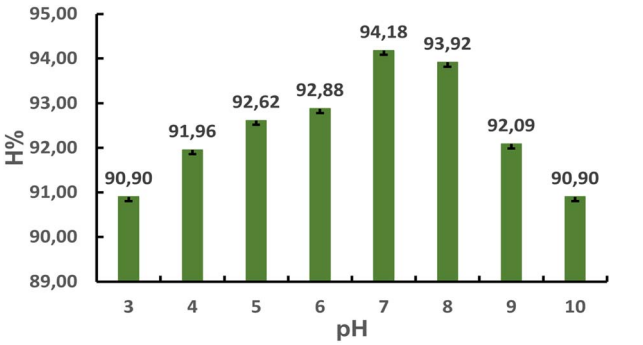

Fig. 8 The dependence of adsorption efficiency (H (%)) on pH.

efficiency was consistently around 99% at various pH levels, except at pH 1, where the efficiency decreased to 87%.

3.2.2. Adsorption equilibrium time. The adsorption process is a dynamic equilibrium, where the adsorbate molecules require a certain period to reach adsorption equilibrium. If the contact time is too short, incomplete adsorption may occur, whereas an excessively long contact time could lead to desorption and unnecessary time consumption. Therefore, the equilibrium time is an essential factor and was investigated following the pH study.

The experimental procedure for evaluating the effect of contact time on the adsorption capacity of the studied material for MB was carried out as described in Section 2.4.2. The time-dependent adsorption results are presented in Fig. 9 and S3 (see SI). The results presented in Fig. 9 and S3 indicate that during the initial 60 minutes, the adsorption process occurred rapidly. This can be explained by the fact that, in this period, MB molecules begin to leave the solution phase, diffuse toward the solid–liquid interface, and bind to the active sites available on the external surface of the adsorbent. The rapid adsorption observed in this stage is primarily due to the abundance of accessible active sites for binding.[41] In the contact time range from 60 to 210 minutes, the adsorption process proceeded at a much slower rate, and the adsorption efficiency remained nearly constant, indicating that equilibrium had been reached. This phenomenon can be attributed to the gradual reduction in the number of available active sites. As these sites became increasingly occupied by previously adsorbed MB molecules, it became more difficult for additional MB molecules to access and bind to the remaining sites due to steric hindrance.[42] Therefore, a contact time of 60 minutes was selected as the optimal adsorption time for MB onto BDSS.

3.2.3. Effect of adsorbent dosage. The effect of adsorbent dosage was investigated. The results of the investigation of adsorbent dosage are presented in Fig. 10 and S4 (SI). As shown in Fig. 10, the adsorption efficiency of MB increased with the rising mass of BDSS.

However, when the adsorbent dosage was increased from 0.05 g to 0.125 g, the improvement in adsorption efficiency was marginal, rising only from 90.09% to 95.73%. Based on this observation, an optimal adsorbent dosage of 0.05 g per 20 mL solution, equivalent to 25 g L^{-1}, was selected for subsequent experiments. The enhancement in MB removal with increasing BDSS dosage can be attributed to the greater availability of active binding sites on the adsorbent surface, which facilitates the adsorption process.[43]

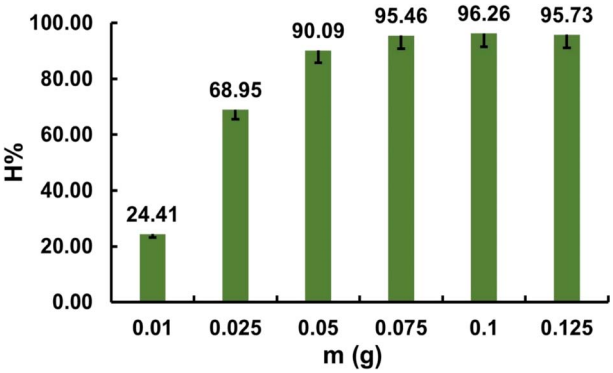

Fig. 10 Effect of adsorbent dosage on adsorption efficiency (H%).

3.2.4. Effect of temperature. The experimental procedure used to investigate the effect of temperature on the adsorption capacity of BDSS for methylene blue (MB) was conducted as described in Section 2.4.3. The results are presented in Fig. 11 and S5.

The results presented in Fig. 11 and S5 show that the adsorption efficiency increased with rising temperature, indicating that the adsorption process is endothermic in nature.[44] This suggests that the adsorption of MB onto BDSS is governed by relatively strong physical interactions, such as hydrogen bonding, along with chemical interactions. On the heterogeneous surface of BDSS, some adsorption sites possess higher activation energies and become more effective at elevated temperatures.

As shown in Fig. 11, when the temperature increased from 313 K to 323 K, the improvement in adsorption efficiency was not substantial. This may be attributed to the increased solubility of MB at higher temperatures, which enhances the interaction between MB molecules and the solvent (H_2O).[45]

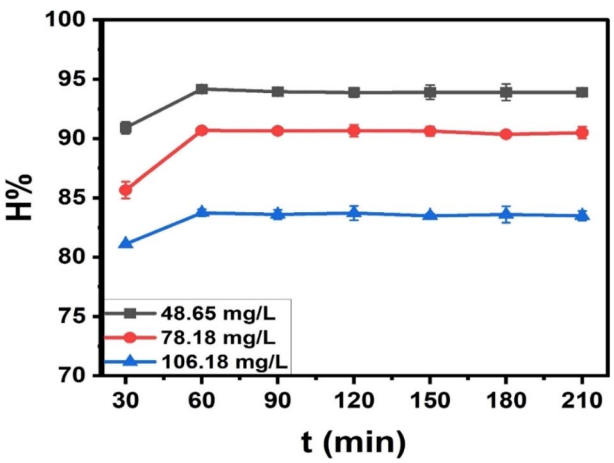

Fig. 9 Effect of contact time on adsorption efficiency (H%).

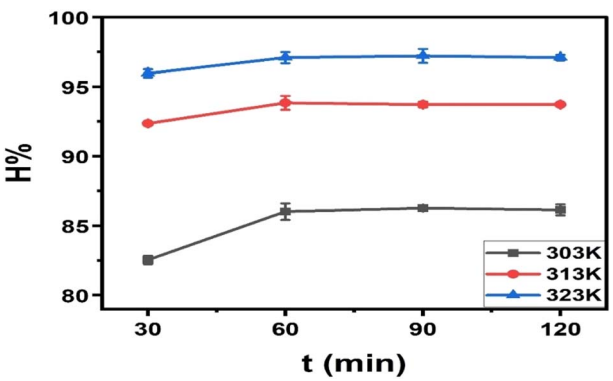

Fig. 11 Temperature dependence of adsorption efficiency (H%).

Consequently, MB molecules become more stabilized in the solution phase, making them less prone to adsorption, despite the increased collision frequency at higher temperatures.[46]

These findings are consistent with previous studies, including the adsorption of MB onto H_2SO_4 (0.1 M)-activated biochar derived from durian shells,[11] nitrogen-rich carbon materials synthesized by co-polymerizing sucrose and urea and subsequently activated with KOH and H_3PO_4,[47] as well as KOH-modified biochar prepared from ball-milled bamboo powder pyrolyzed at various temperatures.[48]

3.2.5. Effect of initial MB concentration. The influence of the initial concentration of methylene blue (MB) on the adsorption capacity of the BDSS material was investigated as described in Section 2.4.4. The experimental results are presented in Fig. 12 and S6 (SI). These figures demonstrate the impact of initial MB concentration on adsorption efficiency. As the initial concentration of MB increases, the adsorption efficiency tends to decrease. This phenomenon can be attributed to the fixed number of available active sites on the adsorbent surface, while the number of MB molecules competing for these sites increases with higher initial concentrations. Consequently, a larger proportion of MB molecules remain unadsorbed.[46]

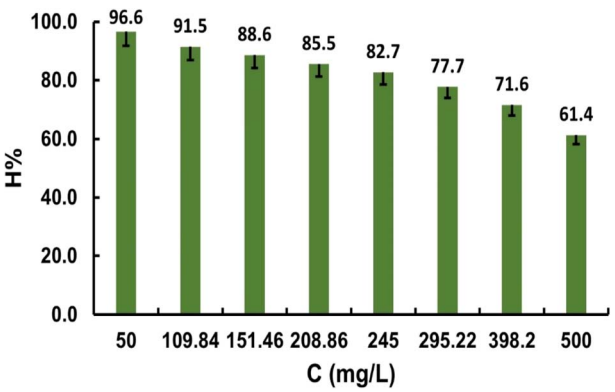

Fig. 12 The relationship between adsorption efficiency (H%) and the initial concentration of MB.

3.2.6. ANN-based simulation of methylene blue adsorption onto durian-derived activated carbon. The dataset was randomly divided into three subsets: 70% for training, 15% for validation, and 15% for testing. The training data was used to fit the network, the validation data was employed to optimize network performance and avoid overfitting, and the test data was used to evaluate the generalization capability of the final model. The hyperbolic tangent sigmoid function (tansig) was used as the activation function in the hidden layer, while a linear transfer function (purelin) was adopted in the output layer to enable continuous output prediction. Fig. 13 depicts the shift in mean squared error (MSE) values against different numbers of hidden layer neurons in the ANN model (from 5 to 20). It is not observed to be monotonic but is found to shift dramatically, indicating the sensitivity of model performance to network structure. Interestingly, sudden peaks in MSE are observed at the 8 and 15 neuron values, suggesting overfitting or non-optimal network structures at these levels. On the other hand, deeper minima in MSE are observed at 11, 14, and 18 neurons, identified by red dashed circles. These network structures had the lowest MSE values and suggest that they provided a better trade-off between the complexity of the network and its capacity to generalize.

Fig. 14 shows with residual plots of the 11 (A), 14 (B), and 18 (C) hidden-layer-neuron ANN models, providing additional diagnostic information to select the number of neurons. Each plot shows the scatter plot of residuals, *i.e.*, calculated minus experimental values, against the model's predicted output. Residuals should ideally be randomly distributed around zero with no systematic trend, indicating the model to be a good fit to the data's underlying structure without bias. As shown, the 11-neuron model (A) has a more compact and even distribution of residuals around zero, suggesting better homoscedasticity as well as less systematic bias. Residuals in the 14 (B) and 18 (C) neuron models (Fig. 14) display wider spreading and more outliers, suggesting reduced predictive accuracy and possible overfitting. Although k-fold cross-validation was not employed, the model was trained using a 70-15-15 split of training, validation, and test sets, and overfitting was mitigated by

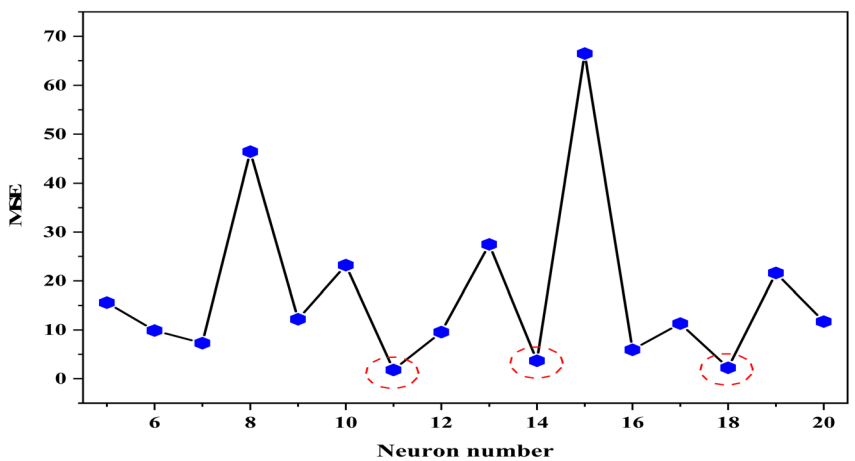

Fig. 13 Mean squared error (MSE) of ANN models as a function of the number of neurons in the hidden layer, from 5 to 20.

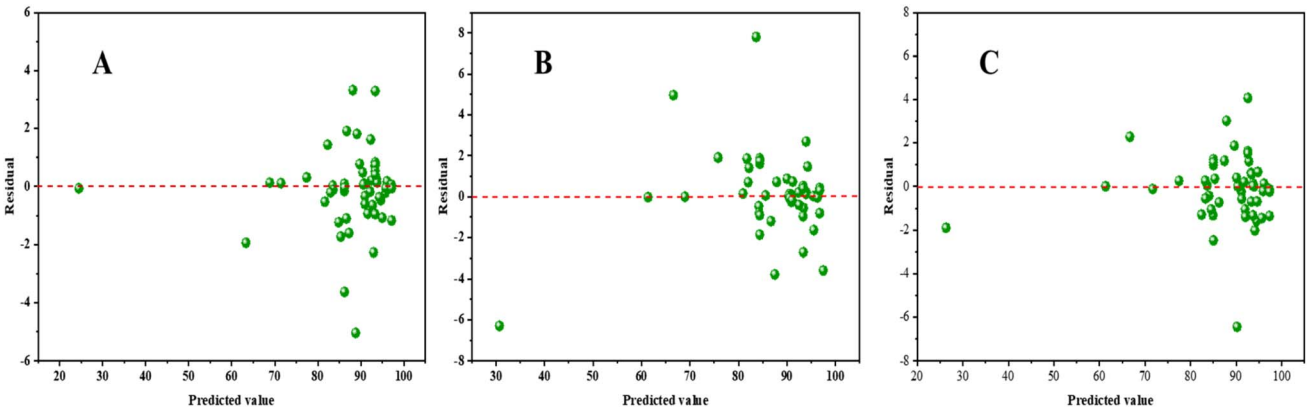

Fig. 14 Residual plots for ANN models with (A) 11 neurons, (B) 14 neurons, and (C) 18 neurons in the hidden layer.

monitoring validation error during training. Moreover, the coefficient of determination (R^2) was used to validate the selection of the neuron numbers. R^2 values were calculated using the following equation:

$$R^2 = 1 - \frac{\sum_{i}^{N} \left(y_{\exp,i} - y_{\mathrm{prd},i}\right)^2}{\sum_{i}^{N} \left(y_{\exp,i} - y_{\exp,m}\right)^2} \quad (13)$$

The calculation shows that R^2 values are 0.986, 0.971, and 0.982 for neuron numbers of 11, 14, and 18, respectively. These are consistent with and coupled with the MSE analysis, indicating the optimal neuron number in the hidden layer.

Fig. 15 illustrates the artificial neural network (ANN) model created to model the adsorption of methylene blue on activated carbon derived from durian waste. The three-layered network consists of an input layer, a hidden layer, and an output layer. Five neurons in the input layer are assigned to each independent factor: pH, contact time, dosage of the adsorbent, solution temperature, and initial dye concentration. These input parameters are linked to a single fully hidden layer consisting of 11 neurons, as identified in performance maximization with MSE and residual analysis. The hidden neurons are linked to an output layer with a single neuron giving the predicted MB removal efficiency. The fully connected feedforward architecture permits the ANN to identify highly nonlinear interaction among input variables and therefore is optimum for adsorption system modeling.

Fig. 16 presents regression analysis of experimental and predicted values for training, validation, and test subsets, and the whole dataset, to confirm the predictive accuracy of the optimized ANN model. The R values were 0.9932, 0.9912, and 0.9955 for training, validation, and test sets, respectively, which reflect very good agreement between target values and network output in all phases. The overall R value of 0.9929 also speaks to the strength of the model's generalization performance. Additionally, linear regression fits (colored lines) track very closely the ideal $Y = T$ line (dashed gray), again speaking to the strength of the ANN in extracting the inherent nonlinear patterns of the adsorption process. The very small deviations from the ideal fit speak to low bias and high predictive homogeneity in all partitions. These results verify that the ANN model is an extremely accurate and effective instrument for predicting

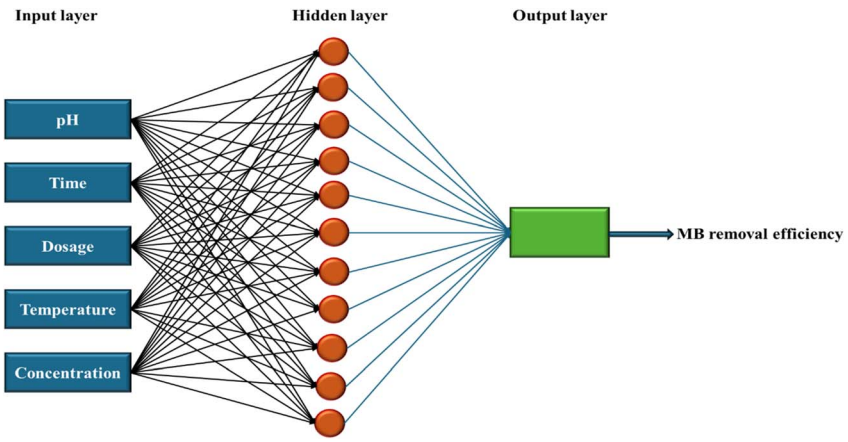

Fig. 15 Schematic of the feedforward ANN architecture comprising five input neurons (pH, time, dosage, temperature, concentration), one hidden layer with 11 neurons, and a single output neuron representing MB removal efficiency.

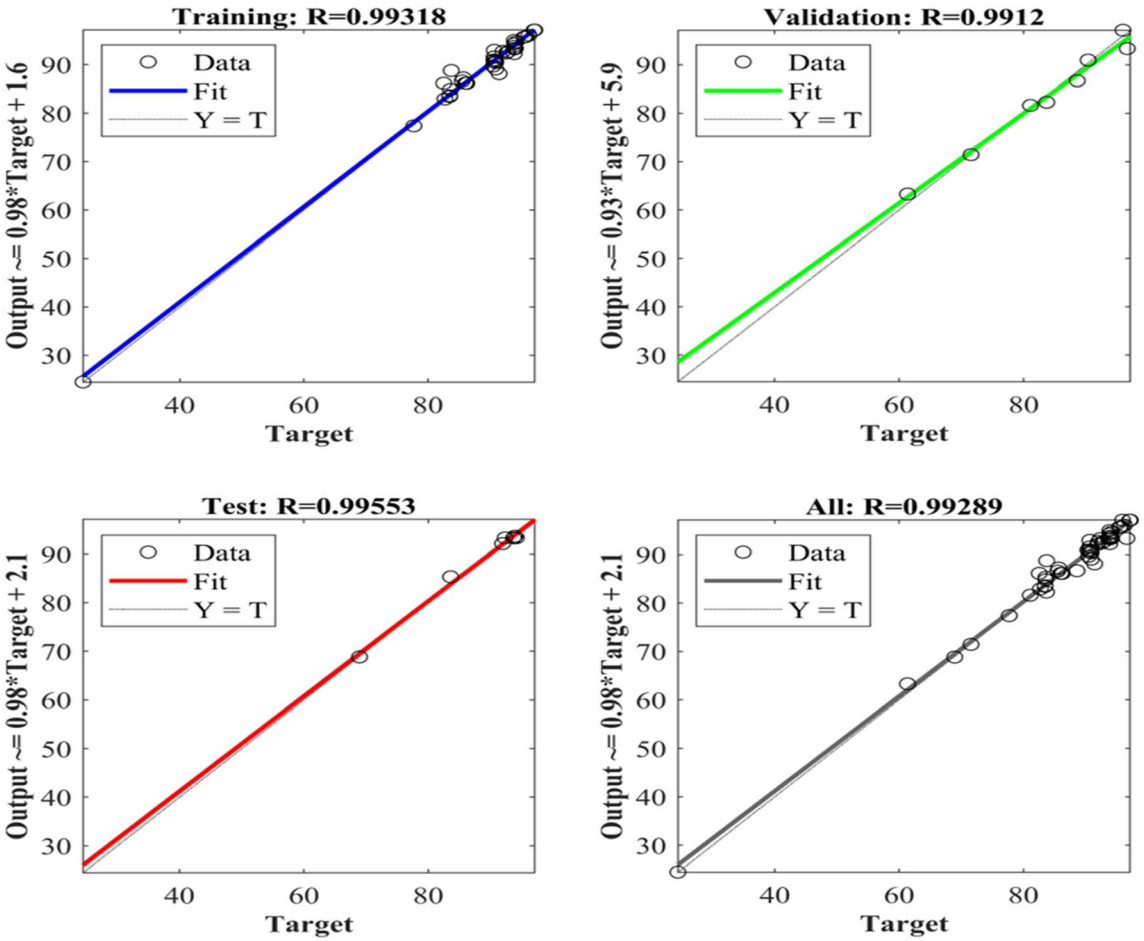

Fig. 16 Regression plots for the ANN model performance on training, validation, testing, and overall datasets. The high correlation coefficients (R > 0.99) across all phases indicate excellent agreement between predicted and experimental values, confirming the robustness and predictive accuracy of the model.

methylene blue adsorption performance under various experimental conditions.

In addition to its prediction capability, the ANN model also gives relative importance (RI), or the ability to ascertain the relative contribution of each input variable to the output. This may be extremely helpful in complex adsorption systems where many factors are nonlinearly interacting. Through observation of the internal weight structure of the network, the ANN can provide quantitative information regarding the strength with which each of the input parameters (*e.g.*, pH, contact time, dosage, temperature, and initial concentration) contributes to the prediction of the target variable, such as adsorption capacity or removal efficiency. This allows the researcher to decide upon the most significant operating parameters, order the process optimization strategies, and achieve mechanistic insight into the system behavior.

Garson's method was applied to measure the relative importance (RI) of each input variable based on the internal weights of the trained artificial neural network (ANN). The method involves decomposing the input layer to hidden layer connection weights and the hidden layer to output layer connection weights. For each input neuron, the absolute product values of its weights to all the hidden neurons and the respective weights of those hidden neurons to the output are calculated. These are summed over all the hidden neurons to yield the total contribution of that input to the output. The RI of each input is then calculated by comparing its contribution to the sum of all contributions from the inputs and expressing it as a percentage. Mathematically, for input neuron i, the RI is calculated as

$$\mathrm{RI}_i = \frac{\sum_{j=1}^{N} |w_{ij} v_j|}{\sum_{i=1}^{M} \sum_{j=1}^{N} |w_{ij} v_j|} \times 100 \quad (14)$$

where w_{ij} is the weight from input neuron I to hidden neuron j, v_j is the weight from hidden neuron j to the output neuron, M is the number of input neurons, and N is the number of hidden neurons. This method allows for the derivation of understandable insight from the ANN model *via* the quantification of the influence of each input parameter on the predicted output.

Fig. 17 indicates the relative significance of each input variable influencing methylene blue removal as determined by

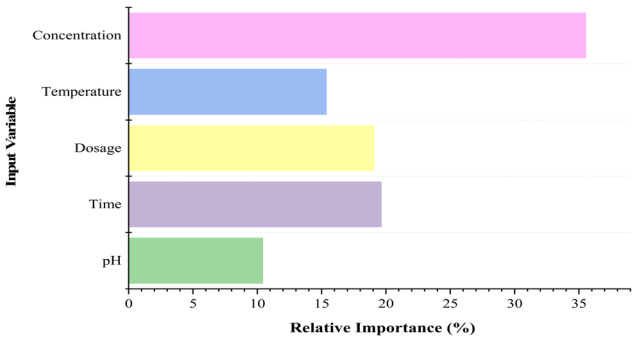

Fig. 17 Relative importance of input variables affecting methylene blue removal, calculated using Garson's algorithm.

Garson's algorithm from the trained artificial neural network model. Among the five input parameters, the initial MB concentration had the greatest RI of 35.52%, indicating that it was the most significant factor in determining adsorption effectiveness. Temperature, dosage, and contact time showed comparatively smaller contributions of 19.63%, 19.08%, and 15.35%, respectively, marking their secondary but distinctive influence on the adsorption process. On the other hand, pH revealed the lowest RI (10.42%), suggesting that it was the least influential parameter of the experimental range being studied. These quantitative variable significance results are a valuable basis for process optimization and further underscore the interpretability benefits of using ANN modeling to model adsorption systems.

3.3. Adsorption isotherm models

3.3.1. Langmuir isotherm model. Adsorption isotherm analysis plays a crucial role in both experimental design and the development of effective adsorbent materials. In this study, the experimental data were evaluated using the Langmuir isotherm model, which is a classical and straightforward approach for describing the equilibrium between adsorbed ions on the solid surface and ions remaining in solution at a constant temperature. The corresponding results are presented in Fig. 18 and 19.

From Fig. 18 and 19, the maximum adsorption capacity was determined to be $q_{max} = 136.99$ mg g^{-1}, with the Langmuir constant $b = 0.046$ L g^{-1}. The adsorption of methylene blue (MB) onto BDSS was found to fit the Langmuir model well, as evidenced by the high correlation coefficient ($R^2 = 0.9908$).

A comparison of the maximum adsorption capacities of MB on biochars derived from agricultural wastes (Table 3) shows that the maximum adsorption capacity (q_{max}) of BDSS is relatively high. Remarkably, it is even higher than that of activated carbon prepared from durian shell pyrolyzed at 600 °C for 2 h and subsequently activated with 0.1 M H_2SO_4 for 24 h.[11]

To assess whether MB adsorption onto BDSS follows a monolayer adsorption process as described by the Langmuir isotherm, the equilibrium parameter (R_L) was evaluated. This parameter is calculated using the following expression:

$$R_L = \frac{1}{1 + bC_0} \quad (15)$$

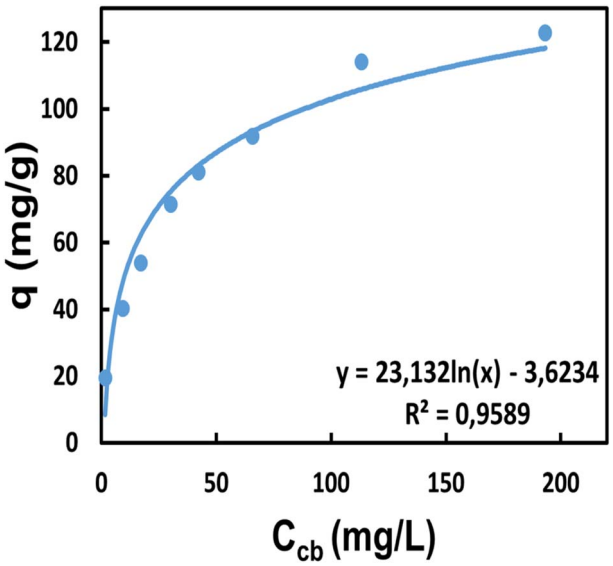

Fig. 18 Langmuir adsorption isotherm.

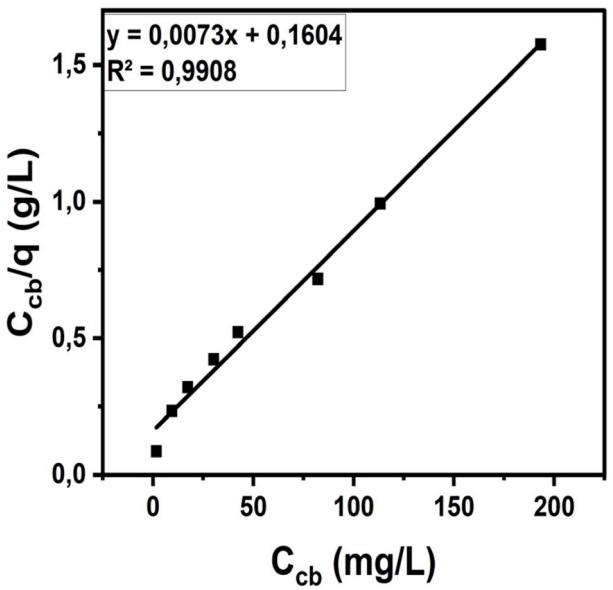

Fig. 19 The relationship between C_{cb}/q and C_{cb}.

where C_0 is the initial dye concentration (mg L^{-1}) and b is the Langmuir constant (L mg^{-1}).

Based on the calculated R_L values shown in Fig. 20, which range from 0.042 to 0.303 (all less than 1), it can be concluded that the Langmuir isotherm model provides a good description of MB adsorption onto BDSS. The adsorption process involves both physical and chemical interactions, occurring predominantly as monolayer adsorption on a homogeneous surface, where each adsorption site accommodates a single molecule and no significant interactions exist between the adsorbed species.

3.3.2. Freundlich adsorption isotherm model. From the experimental results obtained by investigating the effect of

Table 3 Maximum adsorption capacity (q_{max}) of BDSS and other materials

No.	Adsorbent material	Adsorption capacity (mg g^{-1})	References
1	Biochar from *Mimosa pigra*	20.18	49
2	Biochar from elephant dung	34.36	50
3	Biochar from sugarcane bagasse	182.23	51
4	Biochar from rice straw	119.25	52
	Biochar from walnut shell	85.92	52
5	Biochar from durian shell	57.47	11
6	Biochar derived from coconut husk treated with H_2SO_4	88.18	53
	Biochar derived from coconut husk treated with H_3PO_4	92.68	
7	Biochar derived from eucalyptus leaves treated with H_3PO_4	52.18	54
8	Biochar derived from lathyrus sativus husk	98.33	55
	BDSS	136.99	This study

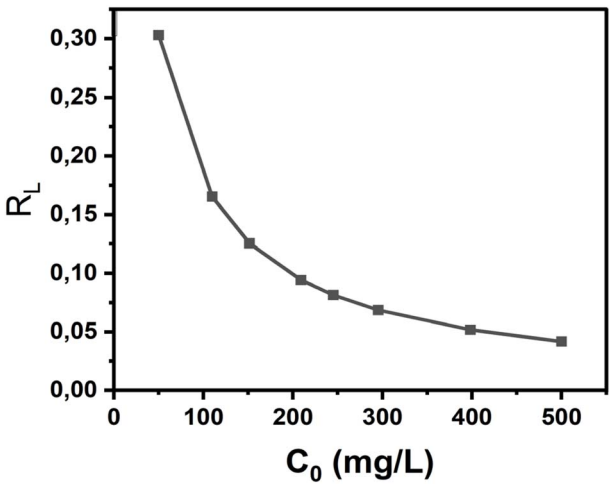

Fig. 20 Dependence of the equilibrium parameter R_L on the initial concentration C_0.

initial MB concentration on the adsorption capacity of the adsorbent, the equilibrium data were further analyzed using the Freundlich isotherm model. The results are presented in Fig. 21. The Freundlich adsorption constant was determined as $K_F = 16.6$ (L g^{-1}) with an exponent of $n = 2.47$, and a high correlation coefficient ($R^2 = 0.9875$) (Fig. 21). The relatively large values of K_F and n indicate the strong adsorption capacity of BDSS and confirm the presence of specific interactions between BDSS and MB molecules. Adsorption occurs on a heterogeneous surface, involving multilayer adsorption without restriction on the number of available sites. The process involves both physical and chemical adsorption mechanisms.

The adsorption of MB on BDSS was found to conform to both the Langmuir and the Freundlich isotherm models. This behavior can be attributed to the hybrid microstructure of BDSS, which contains well-ordered graphitic domains that enable π–π stacking interactions alongside amorphous regions with structural defects. The low crystallinity observed in the XRD pattern and the Raman I_D/I_G ratio of approximately 0.89 provide clear evidence for the coexistence of these two structural features within BDSS.

3.3.3. Dubinin–Radushkevich isotherm model. The results are presented in Fig. 22. As shown, the correlation coefficient obtained from the Dubinin–Radushkevich isotherm model was relatively low ($R^2 = 0.6715$). This indicates that the Dubinin–Radushkevich model does not adequately describe the adsorption of MB onto BDSS.

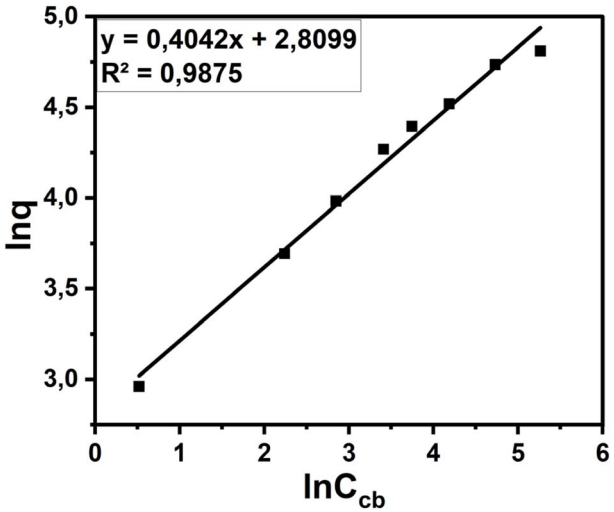

Fig. 21 Relationship between ln q and ln C_{cb}.

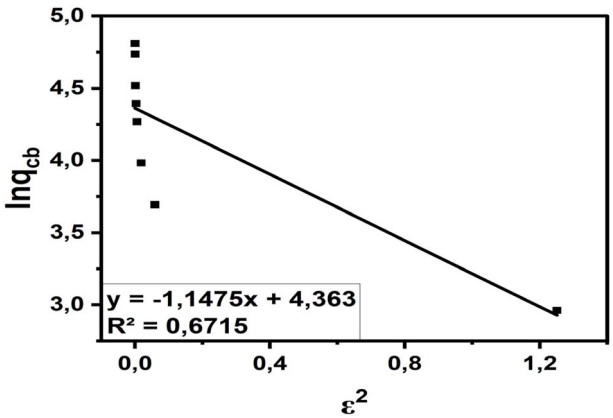

Fig. 22 The relationship between ln q_{cb} and ε^2.

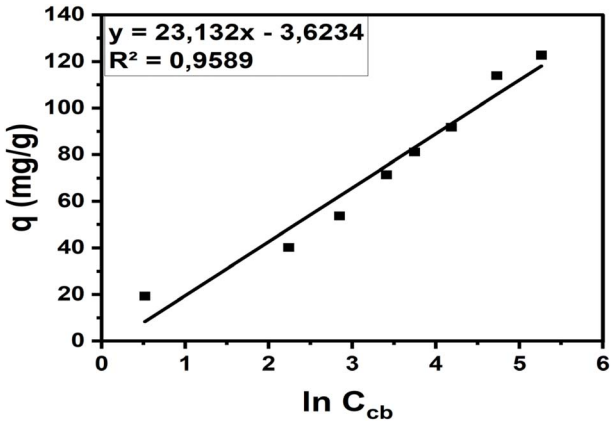

Fig. 23 The relationship between q_{cb} and ln C_{cb}.

3.3.4. Temkin isotherm model. The Temkin adsorption isotherm, which is based on the assumption that the heat of adsorption decreases linearly with coverage due to adsorbate–adsorbent interactions (Temkin and Pyzhev, 1940), was also applied in this study. The results are presented in Fig. 23.

From the results shown in Fig. 23, the determination coefficient ($R^2 = 0.9589$) indicates a good fit of the Temkin isotherm model. The calculated adsorption heat was $b_T = 107.10$ J mol^{-1} (25.59 cal mol^{-1}). According to Ettish *et al.*,[56] physical adsorption is characterized by adsorption heat values lower than 1.0 kcal mol^{-1}, while chemical adsorption typically occurs in the range of 20–50 kcal mol^{-1}. When the adsorption heat lies between 1 and 20 kcal mol^{-1}, both physical and chemical adsorption processes may contribute. Since the adsorption heat of BDSS for MB was well below 1.0 kcal mol^{-1}, the adsorption process can be classified as physical adsorption, confirming that MB adsorption onto BDSS is consistent with the Temkin isotherm model.

3.3.5. Elovich isotherm model. The plot of $\ln(q_{cb}/C_{cb})$ *versus* q_{cb} is presented in Fig. 24. From this plot, the maximum adsorption capacity was determined as $q_{max} = 40.16$ mg g^{-1}, with $K_e = 1.07$, and a correlation coefficient of $R^2 = 0.9653$.

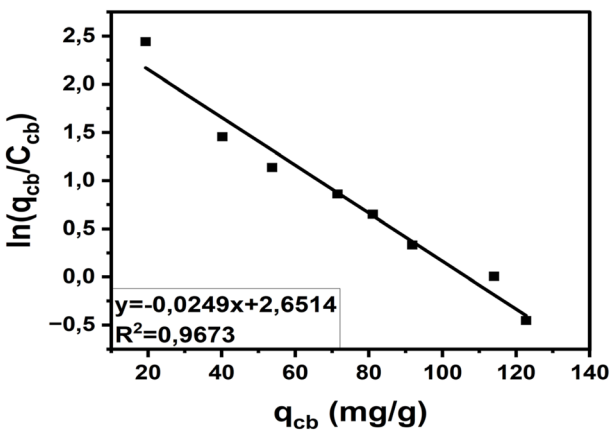

Fig. 24 Relationship between ln (q_{cb}/C_{cb}) and q.

These results indicate that the adsorption of MB onto BDSS is well described by the Elovich isotherm model, suggesting a chemisorption process on a heterogeneous surface, where the adsorption energy varies with surface coverage.

3.3.6. Halsey isotherm model. The plot of q_e *versus* q_e is presented in Fig. 25. The Halsey isotherm model yielded a correlation coefficient of $R^2 = 0.9589$, indicating that the adsorption of MB onto BDSS is well described by this model. This suggests that the process occurs predominantly as multilayer adsorption on a heterogeneous surface and is governed by physical interactions.[57]

From the results presented in Table 4, the determination coefficients (R^2) of the Langmuir, Freundlich, Dubinin–Radushkevich, Temkin, Elovich, and Halsey isotherm models were found to be 0.9908, 0.9875, 0.6715, 0.9589, 0.9673, and 0.9589, respectively. These values indicate that the adsorption of MB onto BDSS is well described by the Langmuir, Freundlich,

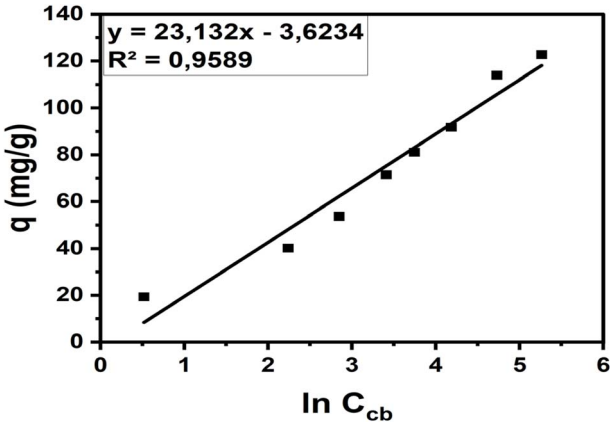

Fig. 25 The relationship between q and ln C_{cb}.

Table 4 Adsorption isotherm constants for the Langmuir, Freundlich, Dubinin–Radushkevich, Temkin, Elovich, and Halsey models

Isotherm model	Constant values	
Langmuir	K_L (L mg^{-1})	0.0978
	q_{max} (mg g^{-1})	136.99
	R^2	0.9908
Freundlich	K_F (mg g^{-1}) (mg L^{-1})$^{1/n}$	16.6
	N	2.47
	R^2	0.9875
Dubinin–Radushkevich	q_{max} (mg g^{-1})	78.49
	β (mol^2 J^{-2})	1.1475
	R^2	0.6715
	E (kJ mol^{-1})	0.66
Tempkin	K_T (L.mol)	1.169
	b_T (J mol^{-1})	107.10
	R^2	0.9589
Elovich	q_{max} (mg g^{-1})	40.16
	K_e	1.07
	R^2	0.9673
Halsey	K_H (L g^{-1})	−0.043
	n_H	1.169
	R^2	0.9589

Table 5 Parameters obtained from the PFO model

MB concentration (mg L^{-1})	$q_{t,exp}$, experimental (mg g^{-1})	$q_{t,cal}$, calculated (mg g^{-1})	Rate constant k_1 (min^{-1})	R^2
48.65	19.168	1.170	0.02645	0.84299
78.18	29.960	2.020	0.01291	0.67063
106.18	40.276	5.790	0.02164	0.99859

Elovich, Temkin, and Halsey models, but not by the Dubinin–Radushkevich model.

Overall, the isotherm analysis demonstrates that MB adsorption onto BDSS involves both monolayer and multilayer adsorption, occurring on homogeneous and heterogeneous surface sites. The process is governed by a combination of physical and chemical adsorption mechanisms.

3.4. Adsorption kinetics

The calculated results based on the PFO model are presented in Table 5 and Fig. 26. Based on the PFO model parameters presented in Table 5 and the kinetic plots in Fig. 26, the correlation coefficients (R^2) range from 0.67063 to 0.99859. Additionally, the equilibrium adsorption capacities calculated from the PFO kinetic model noticeably differ from the experimental values. These results indicate that the PFO model does not adequately describe the adsorption process of MB onto the BDSS material.

As shown in Fig. 27 and Table 6, the equilibrium adsorption capacities calculated from the PSO model closely match the experimental values, and the correlation coefficients (R^2) are approximately equal to 1. These results indicate that the PSO model provides a good fit for the adsorption of MB onto the BDSS material. The average pseudo-second-order rate constant was determined to be 0.0662 min^{-1} L mg^{-1}.

The adsorption process following pseudo-second-order kinetics typically proceeds in two stages. In the first stage, external diffusion occurs, during which MB molecules migrate from the bulk solution to the surface of the BDSS adsorbent. In the second stage, MB molecules attach and adsorb onto the active sites on the BDSS surface. This stage represents the rate-limiting step of the adsorption process. This behavior suggests that the adsorption of MB onto BDSS is predominantly governed by a chemisorption mechanism.

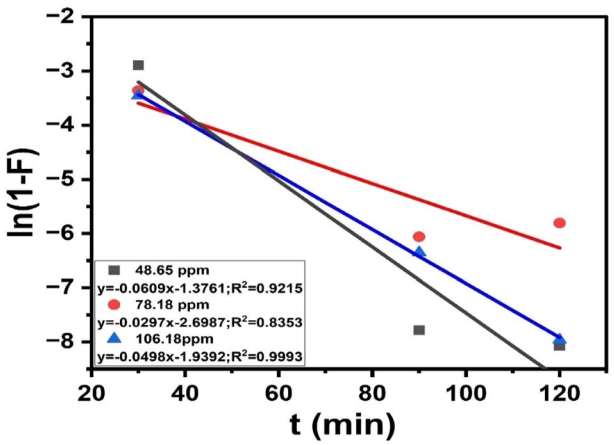

Fig. 26 Pseudo-first-order (PFO) kinetic plots for MB adsorption.

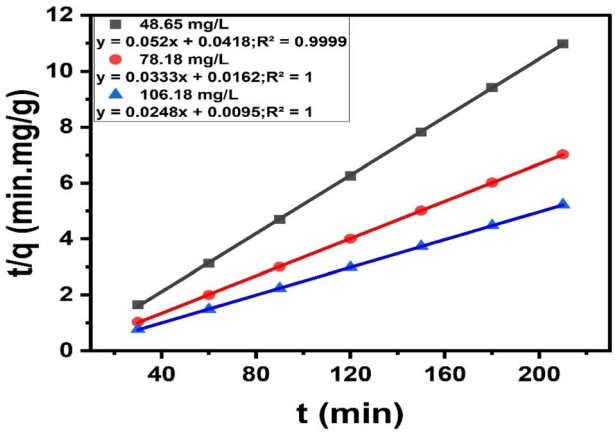

Fig. 27 Pseudo-second-order (PSO) kinetic plots for MB adsorption.

The Elovich kinetic model is commonly applied to describe chemisorption processes on heterogeneous solid surfaces. This model is particularly appropriate in cases where the adsorption rate decreases over time due to surface coverage by previously adsorbed molecules. As illustrated in Fig. 28, the correlation coefficients (R^2) obtained from the Elovich model were relatively low, ranging from 0.5360 to 0.5692. These results indicated that the adsorption kinetics of MB onto the BDSS material did not follow the Elovich model.

The intraparticle diffusion model proposed by Weber and Morris, illustrated in Fig. 29, shows that the plot of q_t *versus* $t^{0.5}$ is divided into two distinct linear regions. This indicates that the adsorption rate is controlled by multiple steps rather than solely by intraparticle diffusion. Intraparticle diffusion is typically influenced by pore size and the pore structure of the adsorbent. The first region exhibits a steeper slope, representing the initial stage where the adsorbate is rapidly transferred from the bulk solution to the external surface and then into the pores of the adsorbent, where adsorption occurs at the active sites. The second region corresponds to the equilibrium stage, during which intraparticle diffusion slows down and gradually reaches equilibrium due to the reduced concentration of MB in the solution.

Moreover, the fact that the linear plots in the first region do not pass through the origin suggests that intraparticle diffusion is not the sole rate-limiting step in the adsorption process.[58] Based on the analyses in Fig. 29, the adsorption mechanism of MB on BDSS can be confirmed as a multistep process: initially

Table 6 Kinetic parameters derived from the pseudo-second-order (PSO) model

MB concentration (mg L^{-1})	$q_{t,exp}$, experimental (mg g^{-1})	$q_{t,cal}$, calculated (mg g^{-1})	Rate constant k_2 (phút^{-1} L mg^{-1})	R^2
48.65	19.168	19.238	0.0646	0.9999
78.18	29.960	30.010	0.0690	1.000
106.18	40.276	40.290	0.0650	1.000

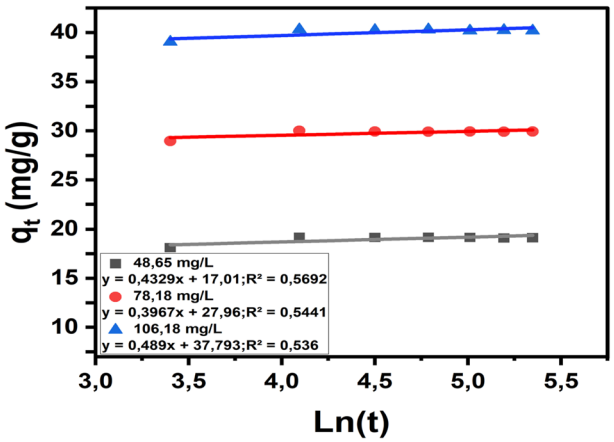

Fig. 28 The relationship between q_t and ln(t).

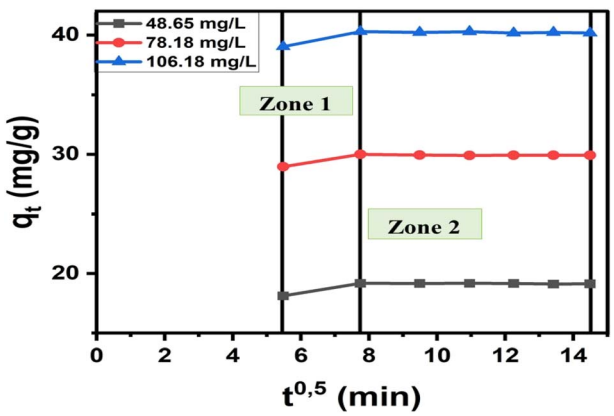

Fig. 29 The relationship between q_t and $t^{0.5}$.

governed by film diffusion, followed by intraparticle diffusion, and ultimately controlled by chemisorption.[59]

Fig. 30 presents the plot of ln(1 − F) as a function of time, which exhibits a linear trend. This indicates that film diffusion is one of the rate-controlling steps in the adsorption process. Film diffusion is typically influenced by the thickness of the boundary layer and the diffusion rate of the adsorbate. It is suggested that the boundary layer surrounding the MB molecules is relatively thick, which hinders the transfer of MB from the liquid phase to the surface of the BDSS adsorbent.

The overall kinetic analysis suggests that the adsorption of MB onto BDSS follows a pseudo-second-order kinetic model and is governed by a combination of intraparticle diffusion, external diffusion, and chemisorption mechanisms.

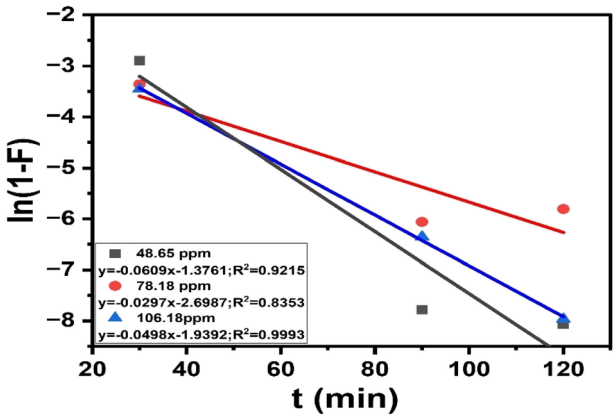

Fig. 30 The relationship between ln(1 − F) and time.

3.5. Thermodynamic analysis

3.5.1. Activation energy. The calculated activation energy and the results are presented in Table 7. The results in Table 7 showed that all activation energy (E) values were less than 25 kJ mol^{-1}, indicating that the adsorption of MB onto BDSS was primarily governed by physical adsorption. In this type of process, van der Waals forces are the dominant interactions. As the initial MB concentration increased from 48.65 to 106.18 mg L^{-1}, the activation energy also increased from 14.65 to 18.32 kJ mol^{-1}. This trend suggests that higher concentrations of MB make the adsorption process more challenging, likely due to increased competition for active sites, which in turn leads to a reduction in adsorption efficiency. These findings are consistent with the earlier results regarding the effect of initial concentration on the adsorption behavior.[60,61]

3.5.2. Adsorption thermodynamics. The thermodynamic parameters for the adsorption of MB onto BDSS were calculated, and the results are presented in Fig. 31 and Table 8.

The thermodynamic parameters summarized in Table 8 revealed that $\Delta G°$ values were negative, indicating that the adsorption of MB onto BDSS was a spontaneous process. Moreover, as the temperature increased from 303 K to 323 K, the $\Delta G°$ values became more negative, decreasing from −2.27 to

Table 7 Activation energy parameters for MB adsorption

MB concentration (mg L^{-1})	Activation energy (E) (kJ mol^{-1})
48.65	14.65
78.18	16.84
106.18	18.32

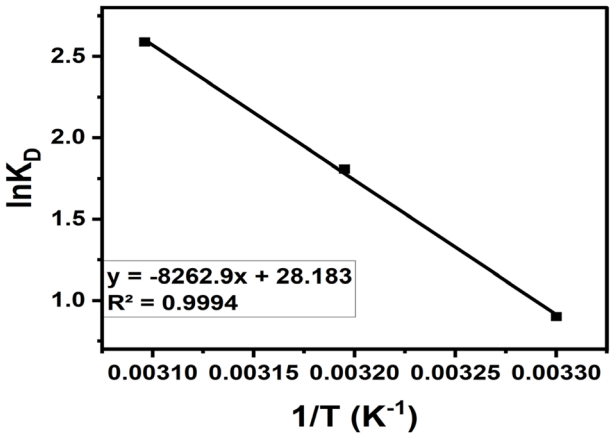

Fig. 31 Plot of ln K_D *versus* 1/*T*.

Table 8 Thermodynamic parameters associated with the adsorption of MB onto BDSS

T (K)	$\Delta G°$ (kJ mol^{-1})	$\Delta H°$ (kJ mol^{-1})	$\Delta S°$ (kJ mol^{-1} K)
303	−2.27	68.70	0.234
313	−4.71		
323	−6.95		

−6.95 kJ mol^{-1}. This suggests that the adsorption becomes increasingly favorable at higher temperatures. In addition, the positive $\Delta S°$ value (0.234 kJ mol^{-1} K) further supports the spontaneity of the process and implies an increase in randomness at the solid–liquid interface during adsorption.

The positive value of the enthalpy change ($\Delta H° > 0$) indicates that the adsorption of MB on BDSS is endothermic in nature and is favored at high temperatures. Foo and Hameed,[58] stated that when $\Delta H°$ is less than 25 kJ mol^{-1}, van der Waals forces are mostly dominant, and the process is a physical adsorption. But between 40–200 kJ mol^{-1}, the chemisorption mechanism dominates. For this study, the calculated $\Delta H°$ value of 68.70 kJ mol^{-1} shows that adsorption of MB on BDSS takes place predominantly by a chemisorption mechanism.

This finding is in accordance with the findings of the isotherm and kinetic analyses, which indicated that the adsorption of MB onto BDSS obeys the Langmuir, Freundlich, Temkin, Elovich, and Halsey isotherm models, and the pseudo-second-order kinetic model. Chemisorption is typically marked by electron transfer or sharing between adsorbate molecules and active sites on the adsorbent surface,[62] but it may also be induced by moderate physical interactions associated with chemical affinity. Furthermore, the calculated enthalpy change is in agreement with the temperature effects found on adsorption performance, which reinforces the finding of the process being thermodynamically viable at high temperatures.

A positive value of $\Delta S°$ indicated that the adsorption of MB onto BDSS was spontaneous and thermodynamically favorable.[63] This can be due to the replacement of water molecules that initially surrounded the MB^+ cations. As the MB^+ ions began to interact with the active sites on the adsorbent surface, these water molecules were released into the bulk solution, where their freedom of movement increased. This release resulted in an increase in the entropy of the system after adsorption and hence the positive entropy change.

However, the relatively small magnitude of $\Delta S°$ suggested that the adsorption of MB onto BDSS did not occur solely through physical adsorption mechanisms.[64] In other words, the process likely involved a combination of both physical and chemical adsorption. This was further supported by the observed increase in adsorption efficiency with rising temperature, characteristic of an endothermic process. Typically, as temperature increases, physical interactions such as van der Waals forces tend to weaken due to the greater molecular kinetic energy, which would reduce the effectiveness of purely physical adsorption. Therefore, if chemical interactions had not been present, the adsorption efficiency would have been expected to decrease at higher temperatures.[46] These findings were consistent with the conclusions drawn from the adsorption isotherm models presented in Section 2.5.

3.6. Proposed adsorption mechanism

The BDSS material possesses an average pore diameter of 4.77 nm, which allows MB molecules to readily access the internal porous structure. Based on the kinetic analysis, the adsorption mechanism of MB onto BDSS can be conceptualized as a process involving both intraparticle and external diffusion (pore filling), which proceeds through four key steps, as illustrated in Fig. 32a: initially, MB molecules migrate from the liquid phase to the interface between the solid phase (BDSS) and the liquid phase. Subsequently, MB molecules approach and adhere to the solid–liquid interface of the BDSS surface.[65] In the third step, MB molecules are transported from the external surface of BDSS to the internal active sites within the porous structure. Finally, MB molecules diffuse into the interior of BDSS particles, reaching the internal adsorption sites. Simultaneously, chemical interactions may occur between the positively charged MB^+ ions and the BDSS surface.[65]

From the results of the pH effect studies, FT-IR analysis, and the known chemical characteristics of MB (a cationic dye containing positively charged nitrogen (N) or sulfur (S) atoms),[65] the following four adsorption mechanisms are proposed for the interaction between MB and BDSS, as illustrated in Fig. 32b: electrostatic interaction (Mechanism I); hydrogen bonding (Mechanism II); electron donor–acceptor interaction (Mechanism III); π–π interaction (Mechanism IV).

As noted by Vargas *et al.* (2011),[66] the presence of surface functional groups plays a crucial role in the adsorption of MB. Specifically, the electrostatic interaction (Mechanism I) can be explained by the attraction between the positively charged nitrogen (N^+) in the MB molecule and the negatively charged carboxylate ions (–COO^-) present on the BDSS surface, as confirmed by FT-IR analysis and illustrated in Fig. 32b (I).

Mechanism II, hydrogen bonding, is commonly observed in most adsorption systems.[48] The formation of hydrogen bonds on the BDSS surface after adsorption was confirmed by FT-IR

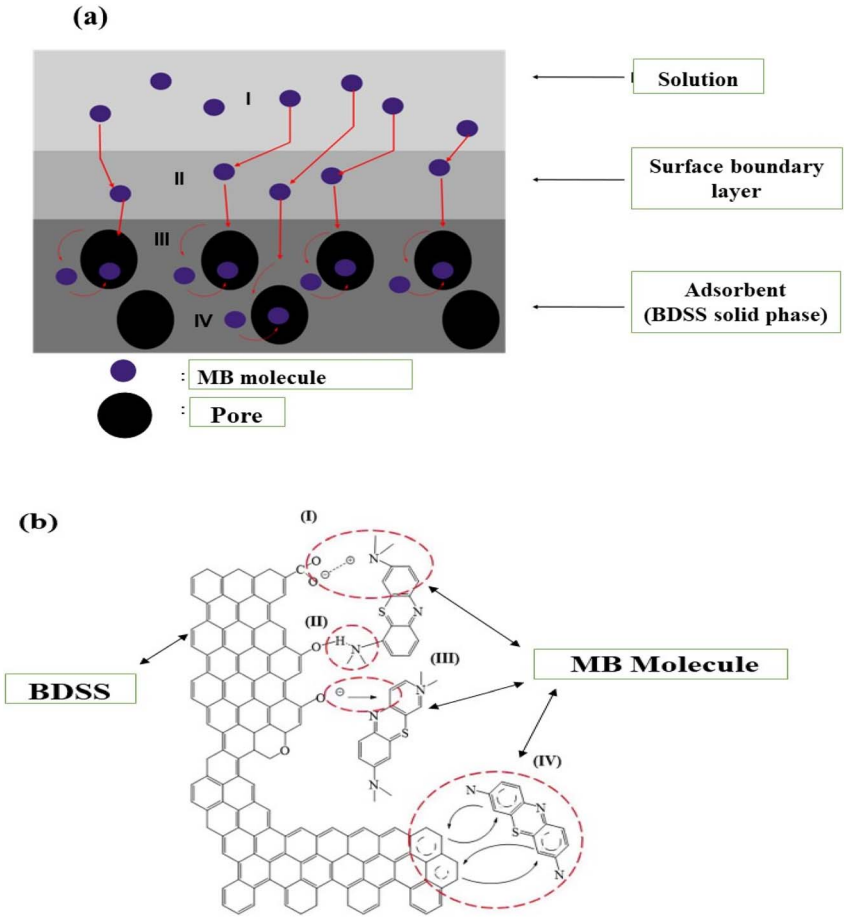

Fig. 32 Proposed schematic illustration: (a) adsorption mechanism of MB molecules *via* intraparticle diffusion and external diffusion; (b) interaction mechanism between MB and BDSS.[67]

analysis. Specifically, hydrogen bonding occurs between the hydrogen atoms of hydroxyl (–OH) groups on the BDSS surface and the nitrogen atoms in the MB molecule, as illustrated in Fig. 32b (II).

Mechanism III involves electron donor–acceptor interactions, where the carbonyl (C=O) functional groups on the BDSS surface act as electron donors, while the aromatic rings in MB molecules serve as electron acceptors, as shown in Fig. 32b (III). The disappearance of the characteristic FT-IR band at 1794.84 cm^{-1}, corresponding to the C=O group after adsorption, further supports this mechanism. These electron donor–acceptor interactions may also lead to the decolorization of MB, converting the dye into its colorless leucomethylene form.[68]

Since MB also contains an aromatic structure, Mechanism IV is proposed to occur through π–π interactions between the benzene rings of MB and the sp^2-hybridized graphite-like carbon network in BDSS, as depicted in Fig. 32b (IV). This mechanism is supported by the disappearance of the FT-IR band at 1474.64 cm^{-1}, which corresponds to the C=C stretching vibration, after adsorption. The pH effect studies on the adsorption of MB by BDSS further confirm the presence of π–π interactions, as the adsorption efficiency was found to be relatively insensitive to pH variations.[48]

The relative contribution of these mechanisms is not fixed but depends on factors such as pH, the degree of aromaticity (sp^2) of BDSS, surface oxidation, and the ionic strength of the solution. A commonly observed order of dominance is: (I) electrostatic interactions ≈ (IV) π–π interactions > (III) electron donor–acceptor interactions > (II) hydrogen bonding.[69]

3.7. Material reusability

The obtained results were compared to the initial adsorption performance of fresh BDSS under the same experimental conditions. As shown in Fig. 33, the BDSS material retained a significant level of adsorption efficiency after three consecutive reuse cycles. Specifically, the adsorption efficiency for MB remained at 84.9% after the first reuse, decreased to 72.9% after the second reuse, and further declined to 53.7% after the third cycle. Although a gradual reduction in adsorption efficiency was observed with each reuse, the material still demonstrated considerable adsorption capacity.

These findings suggest that BDSS has promising reusability potential for wastewater treatment applications, offering the advantage of reducing both operational costs and environmental impacts compared to the use of single-use adsorbents.

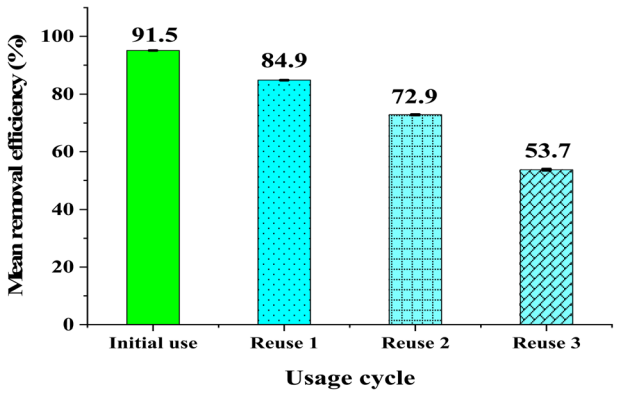

Fig. 33 Reusability performance of BDSS material.

3.8. Disposal and reuse of spent adsorbent

The practical application of adsorbents requires not only high adsorption efficiency but also environmentally responsible post-treatment of the spent material. For the MB-loaded durian peel–seed biochar, several strategies may be considered. First, thermal regeneration (mild pyrolysis or controlled combustion) can desorb MB and restore partial adsorption capacity while also recovering energy. Second, chemical or solvent regeneration (*e.g.*, using dilute acids, bases, or ethanol) may enable multiple reuse cycles, reducing overall material consumption. Third, immobilization or incorporation into construction materials (*e.g.*, bricks, cement composites) offers a safe disposal route by fixing the dye within a stable matrix. These strategies minimize the risk of secondary contamination and extend the sustainability of the adsorbent. Future work will focus on evaluating regeneration efficiency and the environmental footprint of disposal pathways to ensure circular utilization of this biochar.

4. Conclusion

BDSS biochar was produced successfully from durian shells and seeds through pyrolysis at 500 °C in combination with hydrothermal treatment. The BDSS that was obtained had a graphite-like carbon structure with a porous surface, a specific surface area of 441.71 $m^2\ g^{-1}$, an iodine number of 589 mg g^{-1}, and a point of zero charge (pH_{pzc}) of 6.47, indicating good physical properties.

Optimum conditions for the adsorption of methylene blue (MB) from a concentration of 50 mg L^{-1} by BDSS were pH 7, 60 minutes contact time, and an adsorbent dosage of 0.05 g per 20 mL solution.

Adsorption of MB onto BDSS was found to be satisfactorily described using certain isotherm models, including Langmuir, Freundlich, Temkin, Elovich, and Halsey. From the Langmuir isotherm model, the highest adsorption capacity (q_{max}) of BDSS towards MB was 136.99 mg g^{-1}.

Kinetic study showed that the adsorption process followed a pseudo-second-order kinetic model, was spontaneous, and an endothermic process. Monolayer as well as multilayer adsorption was observed, suggesting that the surface of BDSS is both homogeneous as well as heterogeneous in nature. The adsorption process was governed by physical and chemical interactions, in which intraparticle diffusion, external diffusion, and temperature controlled the rate of adsorption.

The primary adsorption mechanisms of MB onto BDSS were electrostatic forces, hydrogen bonding, π–π interactions, electron donor–acceptor interactions, and pore filling. The adsorption efficiency for MB remained at 53.74% following three successive reuse cycles, a result showing the potential for reusability of the material.

In addition, an artificial neural network (ANN) model was also effectively developed for the prediction of BDSS adsorption performance under varying conditions. The feedforward ANN with an optimal topology of five input parameters (pH, contact time, adsorbent dosage, temperature, and initial MB concentration), a hidden layer of 11 neurons, and a single output neuron provided excellent predictive capability ($R > 0.99$ for training, validation, and testing). The model also showed that the initial MB concentration was the most important parameter, followed by temperature, adsorbent dose, contact time, and pH. These results are helpful in process optimization and practical application.

In conclusion, this study confirms that BDSS biochar of durian waste is an efficient, reusable, and stable adsorbent for methylene blue removal. The integration with ANN modeling provides a powerful tool for adsorption behavior prediction and operational condition optimization, forming a very good foundation for further study and practical implementation in wastewater treatment.

Author contributions

Conceptualisation: D. T. H; methodology: D. T. H and N. N. P. N; software: D. T. T. A and N. D. V; validation: D. T. T and N. N. P. N.; data curation: D. T. H. , D. T. T. A and N. N. P. N; writing original draft preparation: D. T. H., V. T. X and N. D. V; writing – review and editing: D. T. H. and V. T. X; visualization: N. N. P. N, V. T. X and N. D. V. All authors have read and agreed to the published version of the manuscript.

Conflicts of interest

The authors declare no conflicts of interest.

Data availability

All data obtained have been included in the manuscript and are available from the corresponding author upon reasonable request.

SI is provided with this article, including additional adsorption performance data of the durian peel–seed biochar. The file contains figures on adsorption efficiency comparison, effects of pH, contact time, adsorbent dosage, and adsorption isotherms at different temperatures and initial dye concentrations. See DOI: **https://doi.org/10.1039/d5ra05313g**.

References

1 N. Nipu, *et al.*, Methylene blue at recommended concentrations alters metabolism in early zebrafish development, *Commun. Biol.*, 2025, **8**, 120, DOI: **10.1038/s42003-025-07471-8**.

2 Z. Cai, *et al.*, Waste-to-Resource Strategy to Fabricate Functionalized MOFs Composite Material Based on Durian Shell Biomass Carbon Fiber and Fe3O4 for Highly Efficient and Recyclable Dye Adsorption, *Int. J. Mol. Sci.*, 2022, **23**(11), 5900, DOI: **10.3390/ijms23115900**.

3 M. M. Hassan and C. M. Carr, A critical review on recent advancements of the removal of reactive dyes from dyehouse effluent by ion-exchange adsorbents, *Chemosphere*, 2018, **209**, 201–219.

4 S. A. Younis, H. A. Maitlo, J. Lee and K. H. Kim, Nanotechnology-based sorption and membrane technologies for the treatment of petroleum-based pollutants in natural ecosystems and wastewater streams, *Adv. Colloid Interface Sci.*, 2020, **275**, 102071.

5 N. S. Topare and S. A. Bokil, Adsorption of textile industry effluent in a fixed bed column using activated carbon prepared from agro-waste materials, *Mater. Today Proc.*, 2020, **43**, 530–534.

6 M. N. Chu, *et al.*, Ce^{3+}/Ce^{4+}-Doped ZrO2/CuO Nanocomposite for Enhanced Photocatalytic Degradation of Methylene Blue under Visible Light, *Toxics*, 2022, **10**(8), 463, DOI: **10.3390/toxics10080463**.

7 A. A. Narvekar, J. B. Fernandes and S. G. Tilve, Adsorption behavior of methylene blue on glycerol based carbon materials, *J. Environ. Chem. Eng.*, 2018, **6**, 1714–1725.

8 R. M. Novais, A. P. F. Caetano, M. P. Seabra, J. A. Labrincha and R. C. Pullar, Extremely fast and efficient methylene blue adsorption using eco-friendly cork and paper waste-based activated carbon adsorbents, *J. Clean. Prod.*, 2018, **197**, 1137–1147.

9 S. Adunphatcharaphon, P. Awanwee, G. Donato, W. V. Vito D'Ascanio and G. Avantaggiato, The Effectiveness of Durian Peel as a Multi-Mycotoxin Adsorbent, *Toxins*, 2020, **12**, 108, DOI: **10.3390/toxins12020108**.

10 A. Putra, *et al.*, Waste Durian Husk Fibers as Natural Sound Absorber: Performance and Acoustic Characterization, *Buildings*, 2022, **12**, 1112.

11 Q. T. Tran, *et al.*, Experimental Design, Equilibrium Modeling and Kinetic Studies on the Adsorption of Methylene Blue by Adsorbent: Activated Carbon from Durian Shell Waste, *Materials*, 2022, **15**, 8566, DOI: **10.3390/ma15238566**.

12 C. D. Sulistiyo, *et al.*, Removal of hexavalent chromium using durian in the form of rind, cellulose, and activated carbon: Comparison on adsorption performance and economic evaluation, *J. Clean. Prod.*, 2022, **380**, 135010.

13 X. J. Gong, Y. S. Li, Y. Q. Dong and W. G. Li, Arsenic adsorption by innovative iron/calcium in-situ-impregnated mesoporous activated carbons from low-temperature water and effects of the presence of humic acids, *Chemosphere*, 2020, **250**, 126275.

14 M. Zhao, Z. Huang, S. Wang, L. Zhang and C. Wang, Experimental and DFT study on the selective adsorption mechanism of Au(III) using amidinothiourea-functionalized UiO-66-NH2, *Microporous Mesoporous Mater.*, 2020, **294**, 109905.

15 J. Wang, *et al.*, Nitrogen-doped carbons from in-situ glucose-coated ZIF-8 as efficient adsorbents for Rhodamine B removal from wastewater, *Microporous Mesoporous Mater.*, 2021, **310**, 110662.

16 E. Díez, *et al.*, A new mesoporous activated carbon as potential adsorbent for effective indium removal from aqueous solutions, *Microporous Mesoporous Mater.*, 2020, **295**, 109984.

17 H. M. Far, *et al.*, Advanced pore characterization and adsorption of light gases over aerogel-derived activated carbon, *Microporous Mesoporous Mater.*, 2021, **313**, 110833.

18 T. Jamnongkan, *et al.*, Study of the Enhancements of Porous Structures of Activated Carbons Produced from Durian Husk Wastes, *Sustainability*, 2022, **14**, 5896, DOI: **10.3390/su14105896**.

19 A. M. Puziy, *et al.*, Porous structure and surface chemistry of phosphoric acid activated carbon from corncob, *Appl. Surf. Sci.*, 2012, **261**, 75–82.

20 H. Wu, Z. Li and H. Liu, Development of carbon adsorbents with high surface acidity and basicity from polyhydric alcohols with phosphoric acid activation for Ni(II) removal, *Chemosphere*, 2018, **206**, 115–121.

21 S. Miskah, T. Aprianti, M. Agustien, Y. Utama and M. Said, Purification of Used Cooking Oil Using Activated Carbon Adsorbent from Durian Peel, *IOP Conf. Ser. Earth Environ. Sci.*, 2019, **396**, 012003.

22 Yuliusman, M. P. Ayu, A. Hanafi and A. R. Nafisah, Activated carbon preparation from durian peel wastes using chemical and physical activation, *AIP Conf. Proc.*, 2020, **2230**, 030020.

23 P. Sriprom, W. Krusong and P. Assawasaengrat, Preparation of activated carbon from durian rind with difference activations and its optimization, *J. Renew. Mater.*, 2021, **9**, 311–324.

24 X. Y. Jiang, Q. Lu, X. C. Dong, B. Hu and C. Q. Dong, Theoretical study on the effects of the substituent groups on the homolysis of the ether bond in lignin trimer model compounds, *J. Fuel Chem. Technol.*, 2016, **44**, 335–341.

25 Y. Wang, *et al.*, Biomass-Based Hydrothermal Carbons for the Contaminants Removal of Wastewater: A Mini-Review, *Int. J. Mol. Sci.*, 2023, **24**, 1769, DOI: **10.3390/ijms24021769**.

26 Z. Xing, *et al.*, Toward Visual Interaction: Hand Segmentation by Combining 3-D Graph Deep Learning and Laser Point Cloud for Intelligent Rehabilitation, *IEEE Internet Things J.*, 2025, **12**, 21328–21338.

27 Z. Xing, *et al.*, Intelligent rehabilitation in an aging population: empowering human-machine interaction for hand function rehabilitation through 3D deep learning and point cloud, *Front. Comput. Neurosci.*, 2025, **19**, 1543643, DOI: **10.3389/fncom.2025.1543643**.

28 I. Anastopoulos, A. Hosseini-Bandegharaei, J. Fu, A. C. Mitropoulos and G. Z. Kyzas, Use of nanoparticles for dye adsorption, *J. Dispers. Sci. Technol.*, 2018, **39**, 836–847.
29 A. M. Awad, *et al.*, Adsorption of organic pollutants by nanomaterial-based adsorbents: An overview, *J. Mol. Liq.*, 2020, **301**, 112335.
30 M. Benjelloun, Y. Miyah, G. Akdemir Evrendilek, F. Zerrouq and S. Lairini, Recent Advances in Adsorption Kinetic Models: Their Application to Dye Types, *Arab. J. Chem.*, 2021, **14**, 103031.
31 F. Mohamed, *et al.*, Activated carbon derived from sugarcane and modified with natural zeolite for efficient adsorption of methylene blue dye: experimentally and theoretically approaches, *Sci. Rep.*, 2022, **12**, 18031.
32 V. Thapliyal, M. E. Alabdulkarim, D. R. Whelan, B. Mainali and J. L. Maxwell, A concise review of the Raman spectra of carbon allotropes, *Diam. Relat. Mater.*, 2022, **127**, 109180.
33 A. C. Ferrari and D. M. Basko, Raman spectroscopy as a versatile tool for studying the properties of graphene, *Nat. Nanotechnol.*, 2013, **8**, 235–246.
34 J. Wang, J. Tu, H. Lei and H. Zhu, The effect of graphitization degree of carbonaceous material on the electrochemical performance for aluminum-ion batteries, *RSC Adv.*, 2019, **9**, 38990–38997.
35 M. Ngabura, S. A. Hussain, W. A. K. Ghani, M. S. Jami and Y. P. Tan, Optimization and activation of renewable durian husk for biosorption of lead (II) from an aqueous medium, *J. Chem. Technol. Biotechnol.*, 2019, **94**, 1384–1396.
36 R. R. Elmorsi, *et al.*, Adsorption of Methylene Blue and Pb 2+ by using acid-activated Posidonia oceanica waste, *Sci. Rep.*, 2019, **9**, 3356, DOI: **10.1038/s41598-019-39945-1**.
37 J. de S. Macedo, *et al.*, Kinetic and calorimetric study of the adsorption of dyes on mesoporous activated carbon prepared from coconut coir dust, *J. Colloid Interface Sci.*, 2006, **298**, 515–522.
38 N. S. Sulaiman, M. H. M. Amini, M. Danish, O. Sulaiman and R. Hashim, Kinetics, thermodynamics, and isotherms of methylene blue adsorption study onto cassava stem activated carbon, *Water*, 2021, **13**, 2936, DOI: **10.3390/w13202936**.
39 J. Wang, J. Ma and Y. Sun, Adsorption of Methylene Blue by Coal-Based Activated Carbon in High-Salt Wastewater, *Water*, 2022, **14**, 3576, DOI: **10.3390/w14213576**.
40 B. Salunkhe and T. P. Schuman, Super-Adsorbent Hydrogels for Removal of Methylene Blue from Aqueous Solution: Dye Adsorption Isotherms, Kinetics, and Thermodynamic Properties, *Macromol*, 2021, **1**, 256–275, DOI: **10.3390/macromol1040018**.
41 H. N. Tran, S. J. You, A. Hosseini-Bandegharaei and H. P. Chao, Mistakes and inconsistencies regarding adsorption of contaminants from aqueous solutions: A critical review, *Water Res.*, 2017, **120**, 88–116.
42 F. Dhaouadi, *et al.*, Adsorption of methylene blue on comminuted raw avocado seeds: Interpretation of the effect of salts *via* physical monolayer model, *J. Mol. Liq.*, 2020, **305**, 112815.
43 A. Hamzezadeh, Y. Rashtbari, S. Afshin, M. Morovati and M. Vosoughi, Application of low-cost material for adsorption of dye from aqueous solution, *Int. J. Environ. Anal. Chem.*, 2022, **102**, 254–269.
44 T. M. Budnyak, *et al.*, Chitosan Deposited onto Fumed Silica Surface as Sustainable Hybrid Biosorbent for Acid Orange 8 Dye Capture: Effect of Temperature in Adsorption Equilibrium and Kinetics, *J. Phys. Chem. C*, 2020, **124**, 15312–15323.
45 P. Senthil Kumar, *et al.*, Effect of temperature on the adsorption of methylene blue dye onto sulfuric acid–treated orange peel, *Chem. Eng. Commun.*, 2014, **201**, 1526–1547.
46 H. Sudrajat, A. Susanti, D. K. Y. Putri and S. Hartuti, Mechanistic insights into the adsorption of methylene blue by particulate durian peel waste in water, *Water Sci. Technol.*, 2021, **84**, 1774–1792.
47 H. Liyanaarachchi, C. Thambiliyagodage, H. Lokuge and S. Vigneswaran, Kinetics and Thermodynamics Study of Methylene Blue Adsorption to Sucrose- and Urea-Derived Nitrogen-Enriched, Hierarchically Porous Carbon Activated by KOH and H3PO4, *ACS Omega*, 2023, **8**, 16158–16173.
48 Q. Ge, *et al.*, Removal of methylene blue by porous biochar obtained by KOH activation from bamboo biochar, *Bioresour. Bioprocess*, 2023, **10**, 51, DOI: **10.1186/s40643-023-00671-2**.
49 N. Xuan Cuong, Study on Adsorption of Methylene Blue from Aqueous Solution by Biochar Derived from Mimosa Pigra Plant, *VNU J. Sci. Earth Environ. Sci.*, 2021, **37**, 43–554.
50 Y. Suma, N. Pasukphun and N. Eaktasang, Adsorption of methylene blue by low-cost biochar derived from elephant dung, *Appl. Environ. Res.*, 2021, **43**, 34–44.
51 W. Zhu, *et al.*, Methylene blue and acid red adsorption on biochar made from modified sugarcane bagasse: A dynamic, equilibrium, and thermodynamic investigation, *Adsorpt. Sci. Technol.*, 2024, **42**, 1–22.
52 M. Hou, *et al.*, Preparation of Biomass Biochar with Components of Similar Proportions and Its Methylene Blue Adsorption, *Molecules*, 2023, **28**, 6261.
53 I. Ghosh, N. Bar and S. K. Das, Methylene blue dye removal by adsorption with coconut coir and acid-treated forms: adsorption-desorption study, MPR and modeling using artificial intelligence, *J. Dispers. Sci. Technol.*, 2024, 1–26, DOI: **10.1080/01932691.2024.2379609**.
54 K. Ghosh, N. Bar, A. B. Biswas and S. K. Das, Removal of methylene blue by H3PO4Treated eucalyptus leaves: Study of fixed bed column and GA-ANN modeling, *Sustain. Chem. Pharm.*, 2022, **29**, 100774.
55 I. Ghosh, S. Kar, T. Chatterjee, N. Bar and S. K. Das, Removal of methylene blue from aqueous solution using Lathyrus sativus husk: adsorption study, MPR and ANN modelling, *Process Saf. Environ. Prot.*, 2021, **149**, 345–361.
56 M. N. Ettish, G. S. El-Sayyad, M. A. Elsayed and O. Abuzalat, Preparation and characterization of new adsorbent from Cinnamon waste by physical activation for removal of Chlorpyrifos, *Environ. Challenges*, 2021, **5**, 100208.

57 M. Davoudinejad and S. A. Ghorbanian, Modeling of adsorption isotherm of benzoic compounds onto GAC and introducing three new isotherm models using new concept of Adsorption Effective Surface (AES), *Sci. Res. Essays*, 2013, **8**, 2263–2275.

58 K. Y. Foo and B. H. Hameed, Factors affecting the carbon yield and adsorption capability of the mangosteen peel activated carbon prepared by microwave assisted K 2CO 3 activation, *Chem. Eng. J.*, 2012, **180**, 66–74.

59 F. Mohammadzadeh, M. Golshan, V. Haddadi-Asl and M. Salami-Kalajahi, Adsorption kinetics of methylene blue from wastewater using pH-sensitive starch-based hydrogels, *Sci. Rep.*, 2023, **13**, 1190, DOI: **10.1038/s41598-023-39241-z**.

60 Ö. Gökçe Kocabay and O. İsmail, Acrylamide based hydrogels in swelling and uptake of methylene blue from aqueous solutions, *Main Gr. Chem.*, 2019, **18**, 281–290.

61 M. A. Al-Ghouti and R. S. Al-Absi, Mechanistic understanding of the adsorption and thermodynamic aspects of cationic methylene blue dye onto cellulosic olive stones biomass from wastewater, *Sci. Rep.*, 2020, **10**, 15928.

62 S. Fan, *et al.*, Removal of methylene blue from aqueous solution by sewage sludge-derived biochar: Adsorption kinetics, equilibrium, thermodynamics and mechanism, *J. Environ. Chem. Eng.*, 2017, **5**, 601–611.

63 H. N. Tran, S. J. You, T. V. Nguyen and H. P. Chao, Insight into the adsorption mechanism of cationic dye onto biosorbents derived from agricultural wastes, *Chem. Eng. Commun.*, 2017, **204**, 1020–1036.

64 N. R. de Mattos, C. R. de Oliveira, L. G. B. Camargo, R. S. R. da Silva and R. L. Lavall, Azo dye adsorption on anthracite: A view of thermodynamics, kinetics and cosmotropic effects, *Sep. Purif. Technol.*, 2019, **209**, 806–814.

65 M. Sulyman, J. Namiesnik and A. Gierak, Low-cost adsorbents derived from agricultural by-products/wastes for enhancing contaminant uptakes from wastewater: A review, *Polish J. Environ. Stud.*, 2017, **26**, 479–510.

66 A. M. M. Vargas, A. L. Cazetta, M. H. Kunita, T. L. Silva and V. C. Almeida, Adsorption of methylene blue on activated carbon produced from flamboyant pods (Delonix regia): Study of adsorption isotherms and kinetic models, *Chem. Eng. J.*, 2011, **168**, 722–730.

67 R. Mohamat, *et al.*, Effectiveness of Porous Durian Shell-based Activated Carbon for Methylene Blue Adsorption, *Int. J. Integr. Eng.*, 2024, **16**, 489–502, DOI: **10.30880/ijie.2024.16.05.037**.

68 M. Ahmad, *et al.*, Turning date palm waste into carbon nanodots and nano zerovalent iron composites for excellent removal of methylthioninium chloride from water, *Sci. Rep.*, 2020, **10**, 16125, DOI: **10.1038/s41598-020-73097-x**.

69 S. Guo, *et al.*, Synergistic effect of hydrogen bonding and π-π interaction for enhanced adsorption of rhodamine B from water using corn straw biochar, *Environ. Pollut.*, 2023, **320**, 121060.